Physics – Uspekhi **61** (11) 1051 – 1071 (2018)

REVIEWS OF TOPICAL PROBLEMS PACS numbers: 61.72.Ff, 61.72.Hh, 62.20.Hg, 63.20.kd, 63.20.kp, **75.80.+q**, 83.60.Np

Nonequilibrium kinetics of the electron–phonon subsystem can give rise to electric- and magnetic-plasticity effects in crystals in alternating electric and/or magnetic fields

V I Karas', V I Sokolenko

DOI: https://doi.org/10.3367/UFNe.2018.06.038350

Contents

Abstract. Kinetic processes in magnetic crystals in an alternating magnetic field and/or a pulsed electric field are studied theoretically, experimentally, and numerically to establish the prime mechanisms by which they influence the structure and the mechanical, dissipative, and magnetic characteristics of crystals. The specific materials studied are severly strained ferritic pearlite steel 15Kh2NMFA and nickel. The paper presents a systematic kinetic analysis of the nonequilibrium dynamics of the electron–phonon subsystem of a magnetic crystal in an electric field. Our proposed method that underlies the analysis solves the system of Boltzmann equations for the electron and phonon distribution functions numerically without expanding the electron distribution function in a power series of the phonon energy. It is shown that an electronic subsystem excited by an electric field transfers energy to the phonon subsystem and thereby massively produces short-wave phonons which act strongly on lattice defects (such as point and linear ones and phase boundaries) and thus redistribute and decrease their density, as well as providing damage healing, decreasing local peak stresses, and reducing the degradation level of construction materials properties. It is found that, under the action of an induction electric field, the electron distribution function becomes nonequilibrium near the Fermi level energy and, as a result of electron–phonon collisions, transfers significant energy to the phonon subsystem, resulting in forming a nonequilibrium phonon distribution function. Based on modified Granato–Lücke and Landau–Gofman models, it is shown, using the calculated phonon distribution function, that the action of phonons on dislocations is much stronger than it would be in the case of thermodynamic equilibrium at the experimentally measured sample heating by 12 K.

V I Karas' National Scientific Center
'Kharkiv Institute of Physics & Technology',
National Academy of Sciences of Ukraine,
Akademicheskaya st. 1, 61108 Kharkiv, Ukraine
V N Karazin Kharkiv National University,
Svoboda sq. 6, 61022 Kharkiv, Ukraine
E-mail: karas@kipt.kharkov.ua
V I Sokolenko National Scientific Center
'Kharkiv Institute of Physics & Technology',
National Academy of Sciences of Ukraine,
Akademicheskaya st. 1, 61108 Kharkiv, Ukraine
E-mail: vsokol@kipt.kharkov.ua

Received 10 August 2017, revised 3 May 2018
Uspekhi Fizicheskikh Nauk **188** (11) 1155 – 1177 (2018)
DOI: https://doi.org/10.3367/UFNr.2018.06.038350
Translated by Yu V Morozov; edited by A Radzig

Keywords: metals, physicomechanical properties, alternating magnetic field, creep rate, magnetic crystal, electron–phonon subsystem, dislocation mobility, nonequilibrium kinetics, magnetoplastic effect, electroplastic effect

1. Introduction

The discovery of magnetoplastic [1, 2] and electroplastic [3–6] effects abbreviated as MPEs and EPEs, respectively, gave an impetus to extensive investigations into the influence of constant and alternating magnetic fields on the structure and mechanical properties of ferro- and antiferromagnets [7]. The observed effects were attributed to variations in dislocation dynamics during their interaction with spin subsystems and changes in barrier characteristics.

Research carried out in the 1960s gave evidence of a sharp decrease of stability to plastic deformations of metals under the action of charged particle fluxes, electromagnetic radiation, or high-density electric current pulses ($J = 10^8 - 10^9$ A m^{-2}). This phenomenon was called the electroplastic effect [3] and found a variety of industrial applications, such as metal drawing, flattening, stretching, stamping, and rolling [4–6]. Experimental studies demonstrated EPE manifestations under various conditions and the dependence of its magnitude on specimen characteristics, including the strain mode and rate, crystallographic structure, temperature, current density amplitude, current direction, pulse length, and frequency.

Certain experimentally observable EPE patterns are most apparent in Zn, Cd, Sn, and Pb single crystals through which pulsed electric current with density $J = 10^8 - 10^9$ A m^{-2} passes during deformation or when they are exposed to accelerated electrons with an energy below the threshold value needed to knock out an atom from the lattice site it occupies in the direction of dislocation glide. This phenomenon manifests itself as a pulsed reduction of deforming stress required to maintain a constant strain rate [3–6].

Single crystals display a strong dependence of the EPE magnitude on the orientation of strained samples. The dependence of the EPE on current density has a threshold character, i.e., it becomes noticeable starting from a concrete value of pulsed current density. This value, in turn, depends on the mode of crystal deformation, its rate, and the temperature. For zinc, for example, the threshold current density at $T = 77$ K ranges $4 \times 10^8 - 5 \times 10^8$ A m^{-2} [5]. A rise in the pulse repetition rate decreases deforming threshold stress and also diminishes the degree of stress relief, whereas a prolonged pulse at a constant current density amplitude increases the stress relaxation depth, as documented in stress relaxation tests and creep studies [3–6]. The main EPE patterns emerging upon deformation of single crystals are still apparent in a weaker form in experiments with polycrystalline materials. However, the EPE magnitude becomes less pronounced as grain size decreases and even disappears in nanocrystals [6]. This means that the EPE is structure-sensitive.

Analogous effects occur during irradiation of materials by bunches of accelerated electron pulses. The combined action of electric current and irradiation by charged particles intensifies the EPE [5].

The influence of a magnetic field on the structure and physical properties of magnetic materials and welded joints subjected to various loadings, such as strain, heating, and radiation, is of great fundamental and applied interest [7–11]. Results of basic research, experimental studies, and numerical simulations of kinetic processes in nonmagnetic crystals placed in a magnetic field are regularly reported in *Physics–Uspekhi* (see, for instance, the review by V I Alshits et al. [12]). Therefore, they are not cited in the present review due to space restrictions.

2. Changes in physicomechanical properties and structure of ferritic pearlite steel 15Kh2NMFA under the effect of severe low-temperature strain in an alternating magnetic field

The objective of this section is to present results of studies on the changes in the structural, mechanical, dissipative, and magnetic characteristics of severly strained ferritic pearlite steel 15Kh2NMFA under the effect of an alternating magnetic field [10,11].

2.1 Material and research methods

A massive specimen of ferritic pearlite steel 15Kh2NMFA [1] subjected to thermomechanical treatment was cut into thin ($h \approx 1$ mm) plates. Some of them were subjected to 57% rolling deformation at $T \approx 90$ K. Both intact and strained plates were used to prepare samples for mechanical testing, with the length $L = 15$ mm of the working part, cross sections $S_1 = 2 \times 0.7$ mm^2 and $S_2 = 2 \times 0.4$ mm^2, and resistance at room temperature of $\sim 3.1 \times 10^{-5}$ Ω cm and $\sim 3.2 \times 10^{-5}$ Ω cm, respectively. The mechanical characteristics of the steel samples before and after deformation, as well as after exposure to an alternating magnetic field $H \| L$, were determined within a temperature range of 138–293 K under a uniaxial stretch at a rate of 10^{-3} s^{-1}. Low-temperature thermostating was performed in a gasoline medium cooled with an accuracy of 0.5 K. The magnetic field was generated by a solenoid calibrated with the use of a Hall sensor. To exclude from consideration Joule heating effects associated with the magnetic treatment, the samples were rinsed thoroughly under running water. Varying the magnetic field strength H in the $4 \times 10^3 - 8 \times 10^4$-A-m^{-1} range and exposure time t allowed the optimal regime to be chosen for the maximum effect of the change in mechanical properties of the strained samples: 4×10^4 A m^{-1}, and $t = 900$ s.

Field dependences of magnetization $M(H)$ were measured at $T = 300$ K by a KRM-Ts-MA magnetometer, with the wide side of the sample oriented normally to the magnetic field. The magnetic characteristics of a given sample were determined before and after magnetic treatment. The coercive force H_c was deduced from $M(H)$ dependences.

Internal friction δ and shear modulus G in different structural states were determined by the inverse torsion pendulum method at a frequency of around 0.5 Hz and temperature from 300 to 800 K.

2.2 Results and discussion

2.2.1 Mechanical characteristics. Table 1 presents initial characteristics of 15Kh2NMFA steel strength (σ_{02} is the conventional yield stress, σ_b is the ultimate strength, σ_f is the fracture stress) and plasticity (ε_u is the uniform elongation, ε_t is the total elongation, ψ is the necking) in the 293–138-K temperature range.

At $T = 293$ K, σ_{02}, σ_b, ε_t, and ψ values are in excellent agreement with the characteristics of this steel according to Quality Specifications 08 93-013-00212179-2003. Strengthening with a reduction in temperature is accompanied by a

[1] The mass-percent chemical composition of 15Kh2NMFA steel in accordance with Quality Specifications 5.961.1106-77 was as follows: C (0.13–0.18), Si (0.17– 0.37), Mo (0.3–0.6), Cr (0.25–0.30), Mo (0.6–0.8), V (0.25–0.30), S ($\leqslant$ 0.025), P ($\leqslant$ 0.025), Cu ($\leqslant$ 0.30), As ($\leqslant$ 0.08), Ni ($\leqslant$ 0.4), and Co ($\leqslant$ 0.025).

Table 1. Initial mechanical characteristics of 15Kh2NMFA steel.

T, K	σ_{02}, MPa	σ_b, MPa	σ_f, MPa	ε_u, %	ε_t, %	ψ, %
293	500	620	1140	7	17	60
273	500	660	1230	7	16	60
258	580	730	1700	6	10	70
218	590	730	2060	6	10	71
138	700	900	2060	6	11	58

decrease in plasticity. Table 1 shows as well that σ_f remains practically unaltered as temperature drops from 218 to 138 K, whereas necking is markedly reduced.

A sharp increase in the yield stress at temperatures below $(0.15–0.2)T_m$, where T_m is the melting temperature, is characteristic of transition metals and alloys with a body-centered cubic (bcc) lattice. This effect is believed to be responsible for a change in the character of the fracture from ductile to brittle fashion in a broad temperature range (see, for instance, Ref. [13]). Under tensile test conditions, the upper boundary T_{vb} of viscous–brittle transition is determined by the onset of a reduction in fracture stress σ_f against the background of some decrease in necking ψ. The factual manifestation of this boundary is represented by the appearance of the signs of cleavage fracture on the fractured surface.

Taking the aforementioned into consideration, it can be supposed that the initial T_{vb} value of 15Kh2NMFA steel lies within the 218–138-K temperature range. The value of σ_f remains virtually unaltered, while ψ decreases by $\approx 18\%$ as the test temperature falls from 218 to 138 K. Therefore, the upper boundary of the brittle–ductile transition can be estimated from the lowest temperature in this range, i.e., $T_{vb} = 138$ K ($-135\,^\circ$C).

It should be noted that the values of ductile–brittle transition temperature T_{x0} determined under the uniaxial tension conditions are lower than those obtained from impact toughness tests, the latter varying significantly in different studies on steel 15Kh2NMFA. Thus, according to work [14], T_{x0} for the 'secondary sorbite' state is $-80\,^\circ$C for small-sized samples, and $-20\,^\circ$C for standard samples. The mechanical characteristics of strained steel are presented in Table 2.

A comparison of the data from Tables 1 and 2 shows that severe low-temperature deformation results in a typical increase in strength, and decrease in plasticity.

As far as the upper boundary of the ductile–brittle transition in strained steel 15Kh2NMFA is concerned, a 17–18% decrease in ψ, identical to that in the initial state, occurs in a temperature range of 168–138 K. Bearing in mind that the tendency toward a reduction in fracture stress at 168 K is accompanied by a decrease in ψ, this temperature can be regarded as the upper boundary of the ductile–brittle transition for a deformed state. In other words, severe low-temperature deformation leads to a noticeable (by at least 30 K) elevation in temperature at the beginning of the ductile–brittle transition.

Table 2. Mechanical characteristics of strained 15Kh2NMFA steel.

T, K	σ_{02}, MPa	σ_b, MPa	σ_f, MPa	ε_u, %	ε_t, %	ψ, %
293	810	910	1590	1.2	2.2	49
273	820	900	1200	1.0	2.0	40
258	880	950	1730	0.8	1.5	50
218	970	980	1920	0.6	1.7	54
198	980	1060	2100	0.5	1.7	54
168	1050	1070	2300	0.5	1.8	45
138	1080	1090	2280	0.5	1.8	39

Table 3. Mechanical characteristics of strained steel 15Kh2NMFA exposed to an alternating magnetic field.

T, K	σ_{02}, MPa	σ_b, MPa	σ_f, MPa	ε_u, %	ε_t, %	ψ, %
293	660	790	1700	0.7	2.4	58
273	670	800	1290	1.3	2.6	43
258	800	920	1880	0.8	2.0	63
218	890	1000	2020	1.2	1.8	60
198	1000	1110	2300	1.2	2.5	66
168	1000	1150	2760	1.3	2.5	60
138	950	1150	2620	1.5	3.0	64

Changes in the mechanical characteristics of strained steel 15Kh2NMFA under the influence of an alternating magnetic field are illustrated by the data in Table 3.

A comparison of the data from Tables 2 and 3 shows that strained samples exposed to an alternating magnetic field are characterized by a much lower yield stress and a higher stress-at-break over the entire temperature range. Specifically, σ_{02} decreases from 810 MPa to 660 MPa, and σ_f increases from 1590 MPa to 1700 MPa, while ψ increases by 20% at $T = 293$ K. A fracturing of the strained specimen after magnetic treatment proceeds with the formation of a cone and a cup ($\psi \approx 64\%$), whereas in the absence of a magnetic field it occurs by shear forming ($\psi \approx 49\%$) (Fig. 1). Even at low temperatures ($T = 138$ K), samples exposed to a magnetic field undergo deformation accompanied by hardening and have a noticeable reserve of plasticity: their total and uniform elongations at $T = 138$ K amount to 3.0 and 1.5%, respectively, versus 1.8 and 0.5% in the strained state.

2.2.2 Internal friction and shear modulus. Material in the initial state does not show anomalous temperature dependences of damping decrement $\delta(T)$ and shear modulus $G(T)$ in the investigated temperature range (Figs 2, 3, curves *1*). At $T = 270$ K, the background level is $\approx 1.5 \times 10^{-3}$. In the 600–700 K range, an insignificant monotonic increase in the background level is observed up to a maximum value below 4×10^{-3}. For $T > 740$ K, internal friction increases exponentially, which can be regarded as a manifestation of the low-temperature branch of the peak located for $T > 800$ K. The shear modulus at $T = 270$ K amounts to 8×10^4 MPa and decreases with a damping factor of $\sim 2.6 \times 10^{-3}$ K^{-1} as temperature increases.

The internal friction background increases markedly for a strained state. In the region of 350–570 K, a broad maximum

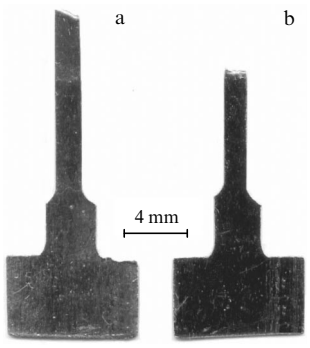

Figure 1. Fracture mode of samples at $T = 300$ K: (a) section (strained state); (b) cup–cone (strained state + magnetic treatment in an alternating field).

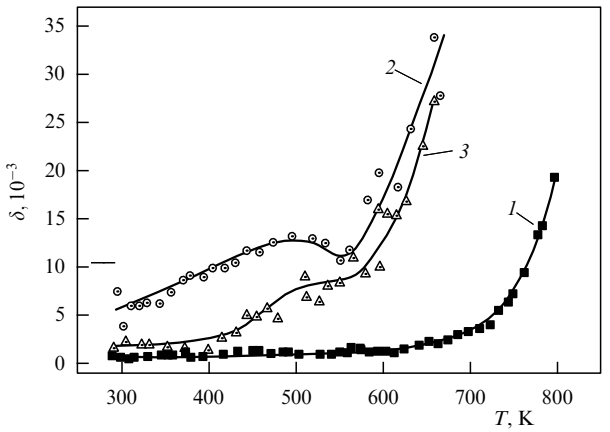

Figure 2. Temperature dependence of internal friction for the steel 15Kh2NMFA in different states: *1* — initial, *2* — after deformation, *3* — after exposure to an alternating magnetic field in the state described by curve *2*.

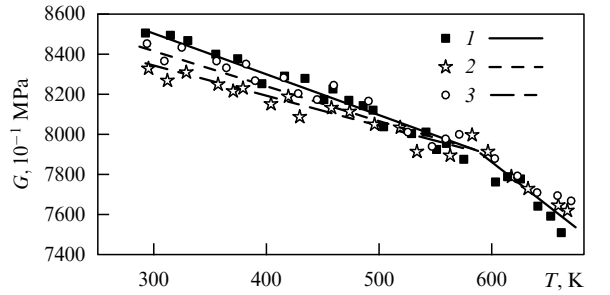

Figure 3. Temperature dependence of shear modulus for the steel 15Kh2NMFA in different states: *1* — initial, *2* — after deformation, *3* — after exposure to an alternating magnetic field in the state described by curve *2*.

of δ is observed, the right branch of which passes to the line of exponential growth of δ (Fig. 2, curve *2*). The shear modulus is reduced by deformation, e.g., by ~ 2000 MPa at $T = 290$ K. At temperatures above 500 K, the strain effect is difficult to identify (Fig. 3, curves *1*, *2*).

Notice that the treatment of the material in the initial state with an alternating magnetic field under the above conditions has practically no influence on the investigated characteristics.

The shear modulus values of the strained samples treated by an alternating magnetic field remain close to those in the initial state over the entire temperature range (Fig. 3, curve *3*). The background internal friction of the treated samples is reduced in the region of 290–420 K (Fig. 2, curve *3*). The broad maximum observed in the strained state degrades, which suggests partial stress relaxation in the material. The magnetic treatment does not stop the exponential growth of internal friction for $T > 550$ K, but causes an appreciable displacement of the growing portion of δ to a higher temperature range, as follows from comparing curves *2* and *3*.

2.2.3 Magnetic characteristics. The field dependence of magnetization $M(H)$ for magnetically treated strained samples gives evidence of an increase in their permeability accompanied by a reduction in the hysteresis loop area previously enlarged as a result of deformation. The obtained

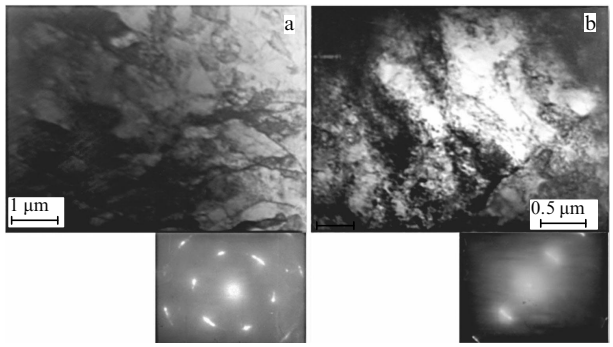

Figure 4. (a) Structure of steel 15Kh2NMFA after rolling deformation at $T = 90$ K. Misorientations between different fragments or cells amount to 6°, and the total misorientation in the microvolume under study reaches 18°. (b) Highly strained structures with elongated dislocations in the form of dense dislocation pileups of the same sign, responsible for a misorientation of up to 19°.

Table 4. Coercive force of steel 15Kh2NMFA in different states.

State	H_c, A m^{-1}
Initial	920.0
After strain	1820.0
After magnetic treatment in an alternating field	1690.0

hysteresis loops are close to the limiting magnetization curves given that the demagnetization factor is taken into account. By way of example, Table 4 presents values of coercive force H_c of the sample. The decrease in H_c reaches $\approx 10\%$ after the magnetic treatment, in comparison with H_c of the strained state before the treatment.

2.2.4 Structure characteristics. Severe low-temperature rolling deformation of steel samples forms a structure highly heterogeneous in terms of the number and type of defects, depending on the orientation of structural elements relative to the rolling plane. Thus, in microvolumes, the orientation of which is only slightly different from the textural one, the sufficiently developed plastic flow is accompanied by the formation of cellular and fragmented structures with a mean lateral size of the cells amounting to 0.25 μm. Misorientations between different fragments or cells amounts to $\sim 6°$, and the total misorientation in the microvolume under study reaches 18° (Fig. 4a).

In microdomains with higher orientation indices, a strongly strained structure was observed with elongated dislocation entities in the form of dense dislocation pileups of the same sign, which cause misorientations of up to 19° (Fig. 4b). This testifies to high elastic distortions of the lattice and incomplete realization of rotation modes to establish textural orientations.

The structure also shows separate high-angle boundaries of a disclination origin with misorientations of $\approx 21°$. The high degree of heterogeneity of the defective structure accounts for the enhanced integral level of internal stresses with their local concentrations both within the finite-sized microregions and at the boundaries between the areas characterized by different degrees of imperfection, as evidenced by dislocation charges at the boundaries and strong blurring of reflections in the electron diffraction patterns, confirming the above discussion.

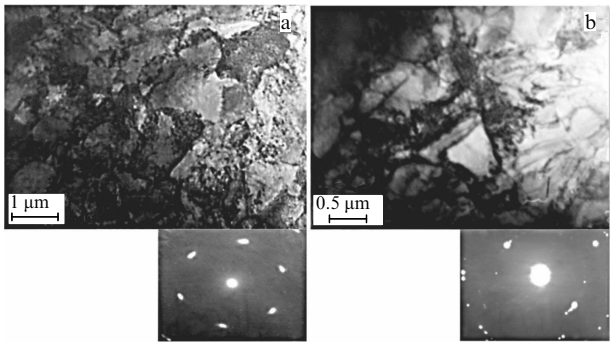

Figure 5. (a) Structure of steel 15Kh2NMFA after rolling deformation at $T = 90$ K and magnetic treatment. (b) Boundary formation at the site of massive pileups of homonymous dislocations.

The imposition of an alternating magnetic field on such a defective structure results in a decrease in the level of internal stresses and equalization of their spectra in the bulk of the material, as a consequence of magnetic relaxation. Pronounced structural changes in domains with a well-developed dislocation structure (cellular ensemble) include an increase in the number of dislocation boundaries associated with a decrease in the average cell size to 0.17 μm, and their misorientation angles to 5° (Fig. 5a).

Effects of plastic relaxation are more pronounced in microvolumes with a higher level of elastic stresses: in domains with local inhomogeneities in the structure, the concentration of internal stresses falls due to dislocation multiplication and redistribution, as well as the dispersal of dislocations directly in the pileups. At the same time, the misorientation angles are reduced to 9°. The boundaries are formed at the sites of powerful pileups of homonymous dislocations (Fig. 5b), which can be interpreted as a manifestation of relaxation. The structural changes in magnetically treated steel match those in the mechanical, dissipative, and magnetic properties.

2.2.5 Possible channels of alternating magnetic field energy absorption. Let us briefly consider possible channels for the absorption of the energy of an alternating magnetic field responsible for relaxation processes in microzones of a ferromagnetic material undergoing severe internal stresses.

The relaxation processes proceed in high-power dislocation pileups and at the interfragment boundaries interacting with magnetic domain boundaries that move under the effect of an external alternating magnetic field. Figure 6 illustrates the potential for relaxation of local internal stresses τ associated with a slowdown of dislocation pileups during the passage across the domain boundary and the reduction in the number of dislocations inside the pileups.

Such 'ejection' of dislocations to the neighboring slip planes is possible due to the generation and motion of double kinks by virtue of nonlinear dislocation dynamics in the field of sign-variable magnetostrictive deformations [15], including domain wall displacement and rotation of the magnetization vector responsible for the effective softening of the elastic moduli [16], which facilitates dislocation migration.

Magnetic relaxation of the orientation aftereffect type [17] promotes the displacement of interstitial impurities and other defects inside the lattice, characterized by local magnetic moments. As a result, partial de-pinning of dislocations and associated point defects fastening them can be expected, in addition to the redistribution and escape of the defects to the interfaces and other preferred sinks, which is likely to result in a lower flow stress. Another stress relaxation channel can be realized through the action of unpinned dislocation sources.

The alternating magnetic field generates an electric field in the conductor volume, in addition to the magnetic component, that acts on the electron subsystem. Lately, the understanding of the mechanisms of the electron subsystem excitation effect on real crystalline solids has received considerable attention [18]: the high-energy electrons appearing under the influence of the electric field interact with phonons and thereby give rise to numerous phonons with energies close to the Debye energy; these phonons, in turn, interact with dislocations and detach them from point defects (stoppers) [19].

In this case, we are dealing with nonequilibrium kinetics (turbulence) in the crystal electron–phonon subsystem exposed to an electric field. Clearly, the state of such a system is far from thermodynamic equilibrium, which prevents its description in terms of temperature and other related characteristics. The description of nonequilibrium systems in the framework of weak turbulence, proposed by V E Zakharov [20, 21], was further extended and elaborated in the work of his disciples (see, e.g., Refs [19, 22–37]).

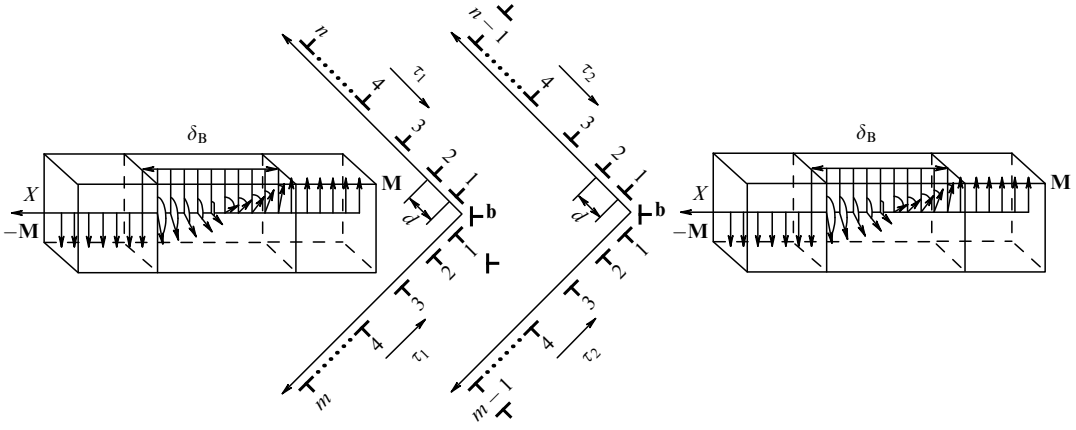

Figure 6. Decrease in the number of dislocations in flat pileups of the Cottrell model during passage across the domain boundary (left to right), corresponding to $\tau_2 < \tau_1$. Arrows in different positions show spin rotation in the Bloch wall of width δ_B (see text).

3. Experimental studies under the creep regime of the peculiarities of polycrystalline nickel plastic flow in an alternating magnetic field at 77 K

This section is designed to report the main results of research on the influence of a harmonic magnetic field and a pulsed magnetic field with different setting times on creep characteristics and their relation to the structural properties of the material of interest. The study object was polycrystalline nickel of 99.99% purity annealed at $T = 900\,^{\circ}\mathrm{C}$ for 2 hours. The experiments were conducted at the transient creep stage in the stepwise loading regime in liquid nitrogen at $T = 77$ K on a test machine with grips and pulls made from a nonmagnetic material [38]. The stress increment at each step was 2–3 MPa; precision of the elongation measurement was $\sim 5 \times 10^{-5}$ cm. Activation parameters and the internal stress level were determined by differential methods as described in Ref. [39]. An electron microscope study of nickel structure defects was carried out before and after the magnetic treatment in an alternating field.

To evaluate the influence of the magnetic field, the test specimen was placed inside a solenoid where a 4×10^4-A-m^{-1} longitudinal constant or alternating magnetic field with a frequency of 50 Hz was created.

An earlier study [2] demonstrated that the exposure to a constant or alternating magnetic field during nickel plastic deformation results in the working of the material. The magnitude of this effect is unrelated to the current creep rate but depends on the loaded stress and applied magnetic field strength. This suggests that the softening effect is largely due to the structure formed by prior strain.

To determine peculiarities of the structure formed in the creep process within the stress range $\sigma \leqslant 0.5\,\sigma_b$, the activation parameters were investigated, which allowed making some conclusions about the type of barriers and mechanisms governing nickel plastic flow during the creep process at 77 K.

Experiments showed that the activation volume and activation energy calculated in the framework of the thermoactivated plastic strain theory are $\sim 0.5 \times 10^{-21}$ cm^3 and 0.14 eV, respectively, and decrease with increasing stress, meaning that the dislocation glide is controlled by defects emerging in the plastic flow process. The total activation energy needed to overcome obstacles is stress-independent and amounts to 0.22 eV. There are a number of obstacles that can influence the low-temperature creep of nickel, which means that they have activation parameters close to those obtained in this study. They are impurities, point strain defects, and forest dislocations.

Because it was experimentally confirmed that the activation volume depends on stress, the impurities do not influence nickel creep at 77 K. At the same time, the concentration of point defects and dislocation density grow with increasing strain; therefore, the activation volume must decrease to agree with experimental data.

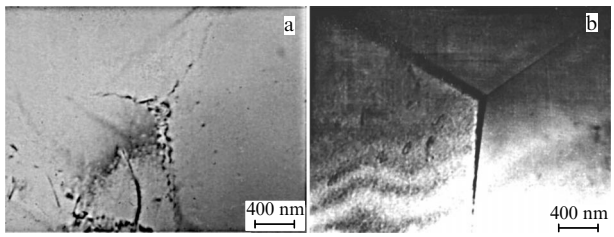

Figure 7. Ni dislocation structure after annealing at 900 °C for 2 hours.

In other words, results of experiments and relevant estimates justify the conclusion that, taking account of intracell dislocation density and point defects (largely interstitial atoms at the initial stages of plastic strain), forest dislocations serve as barriers that control low-temperature nickel deformation.

The mechanism behind activated overcoming these barriers by dislocations is the main mechanism of nickel plastic flow at 77 K. Electron microscopic studies showed that the annealed nickel is characterized by a high degree of structural equilibrium due to recrystallization during annealing, as appears from long smooth traces of the grain boundaries. The dislocation density is around 5×10^8 cm^{-2} (Fig. 7).

Creep at 77 K results in the spatially nonuniform development of material flow and the strong dependence of defect formation on grain orientation relative to the direction of external stress action. For example, some grains display a cellular structure with loose boundaries consisting of 0.5–0.8-μm cells. The mean intracellular dislocation density equals $\sim 2 \times 10^{10}$ cm^{-2}, and mean within-boundary dislocation density is $\sim 9 \times 10^{10}$ cm^{-2}, while the adjacent grains contain massive dislocation pileups with a dislocation density of $\sim 8 \times 10^{10}$ cm^{-2} (Fig. 8). Along with this there are grains that underwent only the initial stages of plastic flow with dislocation glide mostly along the boundaries and piling-up at triple junctions; their dislocation density is $\sim 5 \times 10^{10}$ cm^{-2}.

The main test series with the imposition of a magnetic field on the plastic strain process under creep was carried out according to the following scheme. After load application and achievement of the creep rate of $\sim 5 \times 10^{-6}$ s^{-1}, the magnetic field was turned on and the creep was detected for 180 s. After turning off the field, the creep lasted 180 s more. Then, the sample was additionally loaded again. The investigations were conducted at the transient creep stage with stress

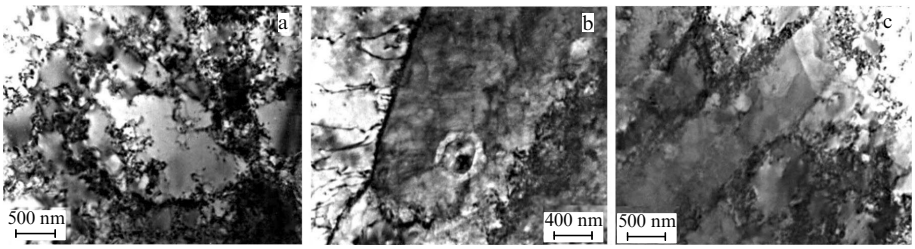

Figure 8. Ni dislocation structure after 9% deformation under stepped creep conditions at $T = 77$ K.

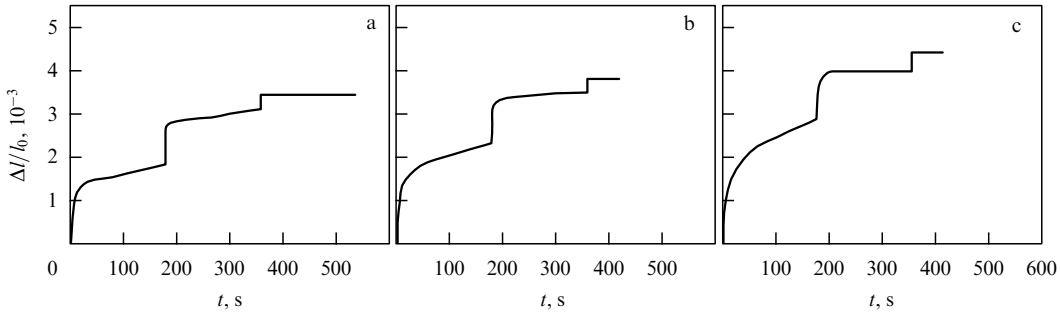

Figure 9. Influence of a 4×10^4-A-m^{-1} constant magnetic field growth time (turn-on time is 1 s) on Ni creep strain at a stable temperature of 77 K and different stresses σ: (a) $0.3\sigma_b$, (b) $0.4\sigma_b$, and (c) $0.5\sigma_b$.

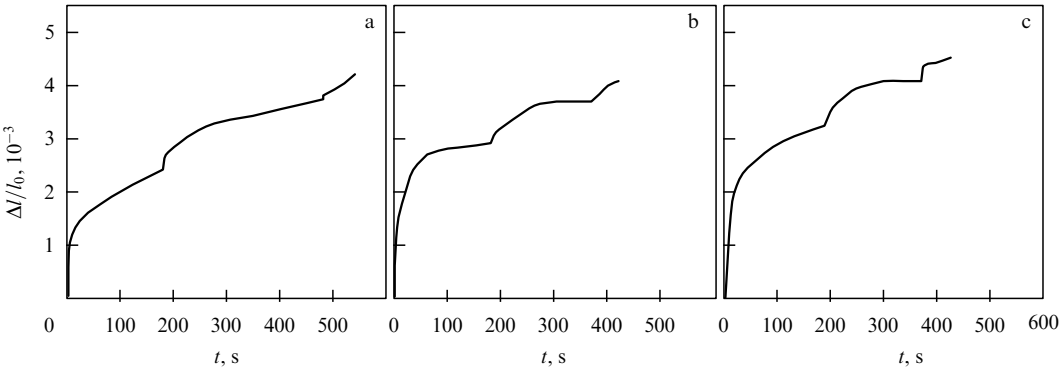

Figure 10. Influence of a 4×10^4-A-m^{-1} constant magnetic field growth time (turn-on time is 60 s) on Ni creep strain at a stable temperature of 77 K and different stresses σ: (a) $0.3\sigma_b$, (b) $0.4\sigma_b$, and (c) $0.5\sigma_b$.

$\sigma \leqslant 0.5\,\sigma_b$. It was found that a 4×10^4-A-m^{-1} constant magnetic field applied in the course of Ni sample creep causes strain increment that continues to grow after the field is turned off.

Figure 9 demonstrates the typical behavior of the Ni creep curves after turning a 4×10^4-A-m^{-1} constant magnetic field on and off at different deforming stresses. Obviously, the shape of the creep curve does not undergo a qualitative change, and creep in the constant magnetic field is described by a logarithmic law. An earlier study [39] revealed the nonmonotonic stress dependence of the softening effect after the imposition of a constant magnetic field. Therefore, we confined our experiments to a small stress region corresponding to the maximum effect.

As is known [39–46], one of the causes of the work softening effect is a rise in sample temperature due to heating with eddy currents. The magnitude of heating depends, all other things being equal, on the rate of the magnetic field variation; its decrease must lessen the effect. To rule out the influence of heating with eddy currents, the sample was cooled in liquid nitrogen and its temperature remained equal to 77 K [47–50].

Figure 10 illustrates time dependence of creep strain after turning on a 4×10^4-A-m^{-1} magnetic field, growing for 60 s. Evidently, the slowly increasing field strength also promotes deformation growth, but the softening effect is much less pronounced than in the case of its rapid (in 1 s) increase (see Fig. 9).

Structural studies showed that imposition of the magnetic field on the creep process has a beneficial effect on the uniformity of dislocation distribution at the early stages of plastic flow, but fails to change the character of structure formation. A cellular structure with dislocation density in the

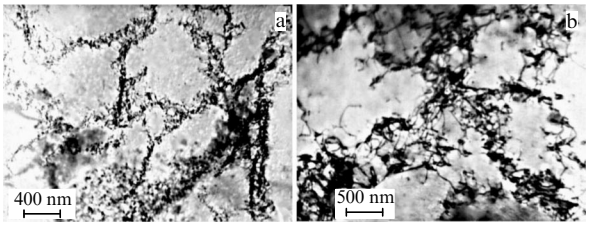

Figure 11. (a) Ni dislocation structure after 9% deformation under stepped creep conditions at $T = 77$ K, and (b) imposition of a pulsed magnetic field with a constant amplitude of 4×10^4 A m^{-1}.

cell body below $\sim 10^{10}$ cm^{-2} forms at a temperature of 77 K, stresses $\sigma \leqslant 0.5\sigma_b$, and a pulsed 4×10^4-A-m^{-1} magnetic field with a constant amplitude.

Dislocations in the cell walls are distributed more uniformly along the boundary, reminiscent of the twist boundary, which suggests the development of a dynamic recovery process (Fig. 11).

The action of an alternating magnetic field during the Ni creep process at $T = 77$ K results in an appreciable increase in the creep rate and deformation. A typical change in the creep curve for $\sigma \leqslant 0.5\sigma_b$ under the effect of an alternating magnetic field with the frequency of 50 Hz and strength $H = 4 \times 10^4$ A m^{-1} is shown in Fig. 12.

The test-time dependence of creep strain after turning on the field, just as after the next added stress, is described by the usual log-law. Clearly, the deformation increases with increasing stress, in agreement with the literature data [43]. Electron microscope studies gave evidence that a harmonic (50 Hz) magnetic field has a much greater effect on the structure of the material than a pulsed field with the same strength amplitude (4×10^4 A m^{-1}). The body of cells is

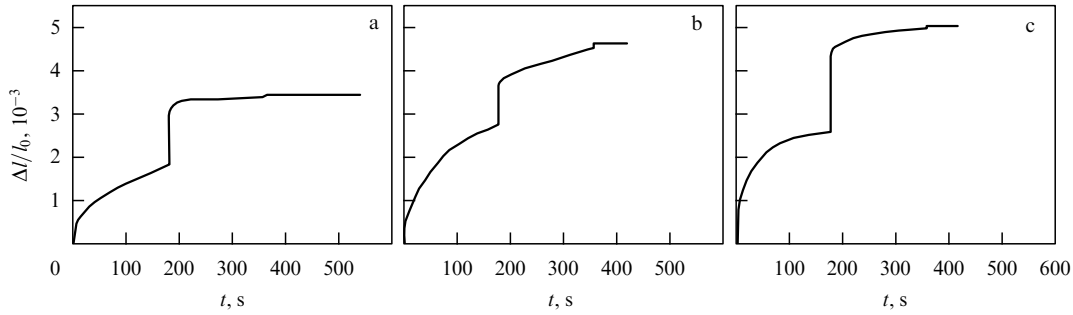

Figure 12. Influence of a 4×10^4-A-m^{-1} harmonic (50 Hz) magnetic field on nickel sample deformation under the creep regime at 77 K and different stresses σ: (a) $0.3\sigma_b$, (b) $0.4\sigma_b$, and (c) $0.5\sigma_b$.

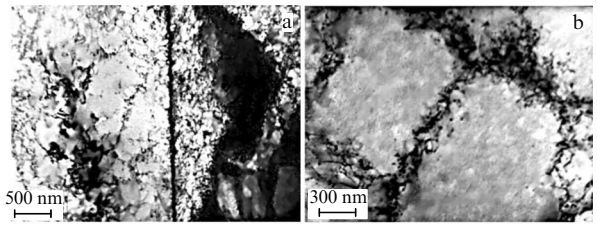

Figure 13. (a) Ni dislocation structure at $T = 77$ K following 9% deformation under stepped creep conditions, and (b) imposition of a 4×10^4-A-m^{-1} harmonic (50 Hz) magnetic field.

practically cleaned from dislocations that concentrate on the boundaries. The dislocation density at the boundaries greatly exceeds 10^{11} cm^{-2}, and powerful dislocation pileups are formed near the grain boundaries (see Fig. 13).

4. Experimental studies under the creep regime of the peculiarities of polycrystalline nickel plastic flow in harmonic and monopolar magnetic fields at the stable 77 K

This section describes the influence of a 4×10^4-A-m^{-1} nonstationary magnetic field and harmonic (50 Hz) and monopolar (50 Hz) fields on Ni creep characteristics [50]. Figure 14 plots the time dependences of deformation in four

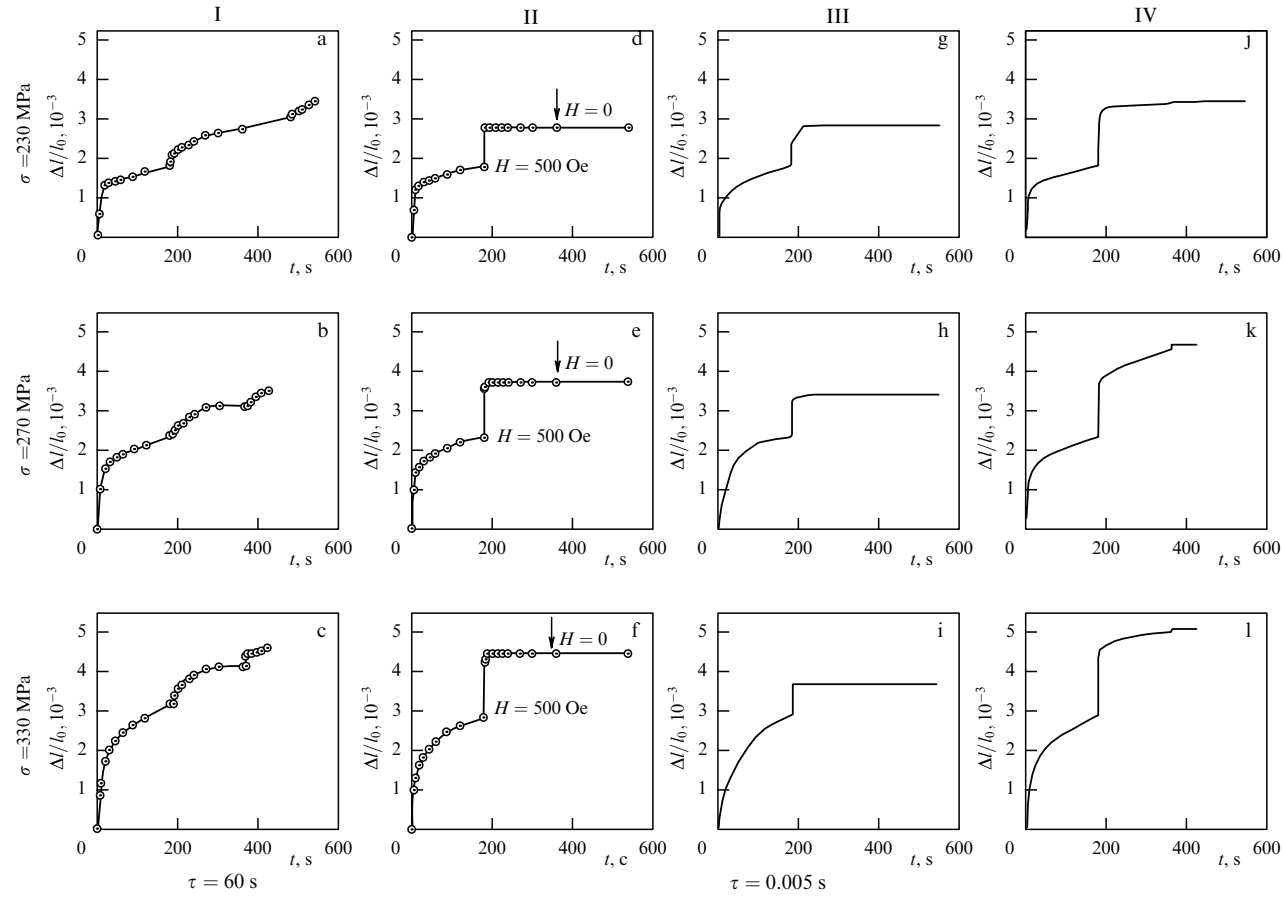

Figure 14. Influence of a 4×10^4-A-m^{-1} alternating magnetic field on Ni creep at 77 K and different stresses for different types of magnetic field pulses τ: (a–c) 60 s (regime I — turning on constant field); (d–f) 0.005 s (regime II — periodic monopolar pulses with sample demagnetization; (g–i) 0.005 s (regime III — periodic monopolar pulses without sample demagnetization, and (j–l) 0.005 s (regime IV — harmonic pulses).

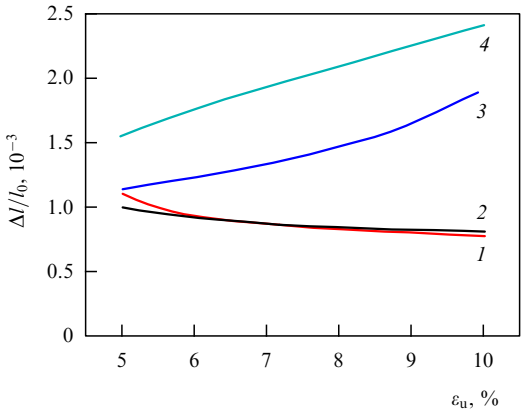

Figure 15. Dependence of polycrystalline Ni softening at 77 K on the degree of strain for different types of 4×10^4-A-m^{-1} magnetic field pulses with different growth times τ: 1s (turning on constant field) (curve *1*); 0.005 s (periodic monopolar pulses without sample demagnetization) (curve *2*); 0.005 s (periodic monopolar pulses with sample demagnetization) (curve *3*), and 0.005 s (harmonic pulses) (curve *4*).

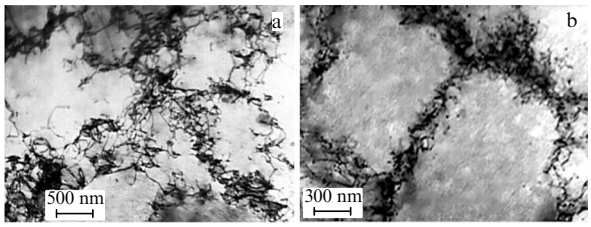

Figure 16. Ni dislocation structure following 9% deformation under stepped creep conditions at $T = 77$ K and imposition of a 4×10^4-A-m^{-1} nonstationary magnetic field with different growth times τ: (a) 60 s (single pulse), and (b) 0.005 s (periodic monopolar pulses).

regimes (I–IV) of turning on a nonstationary magnetic field with different growth times τ: Figs 14(a–c): 60 s (turning on constant field); (d–f): 0.005 s (periodic monopolar pulses with sample demagnetization); (g–i): 0.005 s (periodic monopolar pulses without sample demagnetization, and (j–l): 0.005 s (harmonic pulses). Figures 14a, d, g, j correspond to stress $\sigma = 0.3\sigma_b$, Figs 14b, e, h, k to $\sigma = 0.4\sigma_b$, and Figs 14c, f, i, l to $\sigma = 0.5\sigma_b$.

The time dependences of deformation in all four regimes of turning on the nonstationary magnetic field under creep conditions were measured in response to the stepwise increase in stress $\sigma = 0.3\sigma_b$ (Figs 14a, d, g, j), $\sigma = 0.4\sigma_b$ (Figs 14b, e, h, k), and $\sigma = 0.5\sigma_b$ (Figs 14c, f, i, l), without changing the samples and regimes. Therefore, the action of an identical monopolar magnetic pulse in regimes II and III caused, owing to demagnetization in regime II preceding each subsequent increase in stress, different deformations of the samples (see Figs 14 and 15). The difference in the sample strains was due to a significantly higher inductive electric eddy field in regime II than in regime III. Experiments showed that only a slow turning on and off of the stationary 4×10^4-A-m^{-1} magnetic field increased deformation of Ni samples under creep conditions. The growth of sample deformation induced by rapid turn-on of the field under the same conditions (Figs 14d–i) was soon arrested without a rise in stress. The deformation did not increase at all after the rapid switch-off of the magnetic field.

Figure 15 illustrates a manifestation of the softening effect in different strained states of polycrystalline nickel resulting from the exposure of the sample in the creep regime to magnetic field pulses of equal strength (4×10^4 A m^{-1}) differing in the growth time τ. It follows from Fig. 15 that softening under the influence of monopolar pulses without sample demagnetization and of a constant magnetic field with a growth time of 1s is practically identical in a wide range of degrees of creep strains. At the same time, softening under the action of harmonic pulses markedly increases with strain intensity, as it does in the case of periodic monopolar pulses with sample demagnetization in response to a short pulse series.

Electron microscopic studies showed that a nonstationary magnetic field influences the material structure more strongly the shorter the field growth time is (Fig. 16). The body of cells is cleaned from dislocations that concentrate only at the boundaries (Fig. 16b). Dislocation density at the boundaries greatly exceeds 10^{11} cm^{-2}, and large dislocation pileups are formed near the grain boundaries (Fig. 16b).

5. Electroplastic effect in metals

One of the objectives of the study undertaken by V I Spitsyn and O A Troitskii [51] (see also monograph [6]) was to elucidate in experiment if variations of the electron energy spectrum in metal crystals change their strength and plasticity, bearing in mind that these properties had always been thought to depend only on the mutual position of atoms, oscillations in the lattice, interactions between dislocations, etc.

The main difficulty encountered in such experiments is the impossibility of influencing the electron subsystem without changing the lattice subsystem and heating of the metal. Other difficulties are related to the limitation on electron drift velocities arising, paradoxically, from the high conductivity of metals. It follows from very general physical considerations that electron–dislocation interactions must occur in metal crystals. This means that the influence of a change in the electron subsystem state on dislocation motion and interactions (hence, the plastic and stress–strain properties of the crystals) can be studied in experiment.

The application of an electric field to a metal induces current. At current densities above ~ 1 A mm^{-2}, samples are noticeably heated up, but the use of a pulsed current allows the density to be increased by a few orders of magnitude and keeping the practically cold metal. This approach was employed in a series of experiments designed to observe the influence of electric current on metal plastic deformation under conditions uncomplicated by sample heating [51].

The authors of Ref. [51] were the first to employ another approach consisting in the injection of accelerated electrons into a metal undergoing deformation. It resulted in the excitation of plasma electron oscillations and, as expected, electron–dislocation interactions analogous to current–dislocation interaction. In this case, electrons with an energy below the atom knocking-out threshold are mostly used, which prevents the genuine radiation action exerted by radiation defects in the lattice (metal strengthening and plasticity impairment) at low temperatures due to dislocation blockade by point defects and their ensembles or, vice versa, softening at moderate and high temperatures by virtue of the thermal motion of radiation defects.

These methods allowed a new phenomenon to be discovered, called the electroplastic effect (EPE) by the

authors of Ref. [51]. The essence of the effect is as follows. Plastic resistance of metals decreases as energy is transferred to the electron system; in other words, the metals undergo plasticization. It turned out that metal crystals either stretched or contracted at a constant rate or subjected to a creep test under constant mechanical stress are disordered in response to electric current and irradiation. The maximum magnitude of the effect amounts to a few dozen percent.

The dependence of the effect on temperature, accelerated electron energy, current density and frequency was investigated. A rise in temperature was shown to weaken the effect, even if insignificantly. It became heightened as current density and frequency, as well as the energy of accelerated electrons injected into the deformable metal, increased. However, overshooting the atom knock-out threshold resulted in metal strengthening instead of plasticization (at low temperatures), i.e., inversion of the above effect related to the usual radiation action took place.

The use of a double sample with a deformable (I) working part and nondeformable (II) part makes it possible to distinguish between the two effects of electric current. Pulsed current passing through part I decreases deforming force ΔP_{I} due to the combined action of the current and pinch-effect (magnetostriction by the sample's magnetic field). When the pulsed current passes through part II, the decrease in ΔP_{II} is attributable to the pinch effect alone; the difference between ΔP_{I} and ΔP_{II} can be regarded, in the absence of current-induced heating, as true electroplastic deformation of the sample. The experimental data reported in Ref. [51] suggest three types of the mechanism underlying the electroplastic effect. As noted above, its magnitude increases in proportion to current density and accelerated electron energy. Therefore, it can be assumed to relate to 'electron wind' generation in the metal lattice and the development and enhancement of electron acceleration of moving dislocations. Such an assumption agrees well with experimental observations, except for data on the influence of alloying.

It was shown that EPE is more pronounced in alloyed samples than in 'pure' metals. If it were totally determined by dislocation acceleration, i.e., 'electron wind', it would be natural to expect its decrease rather than increase in an alloyed metal having more obstacles to dislocation motion in the form of impurity atoms. This means that the dependence of the effect on impurity content of metal is in conflict with the described mechanism.

Another possible mechanism is postulated based on the assumption that electron excitations (the 'electron wind' in the case of electric current contribution and electron plasma oscillations in the case of radiative approach) cause changes to the dynamics of oscillating dislocation segments and thereby shorten the time needed for dislocations to overcome the obstacles and dislocation pileups to break away from them. The authors of Ref. [51] described this mechanism as more realistic. They presented current-strength dependences of deforming force decrement ΔP and sample length increment ($\Delta l \times 10^3$ mm) resulting from the passage of single electric pulses through both pure and alloyed zinc crystals. Alloying was shown to increase the threshold current density values, starting from which deforming force oscillations develop and the current dependence becomes steeper.

The cause of these changes is either altered electric interaction between charged impurities and dislocations in the metal or anharmonic thermal fluctuations of dislocation segments related to their active damping by conduction electrons or electron plasma oscillations, i.e., as a result of the direct electron–dislocation interaction that occurs on dislocations being found on the verge of breakaway from the obstacle (especially on the heading dislocations in pileups) rather than on moving dislocations.

The mechanism of changing electric interactions between charged impurities and dislocations is invalid, because the effect being considered takes place not only under the influence of the current but also due to irradiation when no potential is applied to the sample that could change the dislocation–impurity interaction.

The dependence of the electroplastic effect on the presence of impurities in metal and on the pulsed current frequency provides evidence in favor of the mechanism of electron damping of dislocation segments. Indeed, in alloyed samples, the number of critical regions in a loaded crystal, in which dislocations are on the verge of breakaway, increases along with the number of dislocation pileups discharging upon the detachment of heading dislocations from the obstacles. This makes clear the cause of the frequency dependence of the effect; namely, the enhanced current pulse repetition rate contributes to the increase in the frequency of electron impacts on dislocation segments and in the frequency of attempts to overcome obstacles by dislocations. Moreover, this mechanism accounts for the dependence of the effect on current density and the energy of accelerated electrons (in the case of irradiation). Specifically, the increased intensity of electron impacts makes possible a shortening of the time needed for dislocations to overcome an obstacle.

To sum up, the model proposed by the authors of Ref. [51] to explain the electroplastic effect reduces to the following. Electric current or electron plasma oscillations (in the irradiation method) alter the interaction between dislocations and their pinning centers due to active electron damping of oscillating dislocation segments, to the manifestation of anharmonicity in their thermal fluctuations, and the enhanced probability of overcoming obstacles by dislocations (shortening of time needed for the dislocations to overcome an obstacle). Therefore, experiments on sample stretching (contraction) at a constant rate demonstrate a reduction in the deforming force, whereas those with relaxation of applied stresses and creep reveal an increase in the relaxed stress component and the creep relaxation rate, respectively.

The temperature dependence of electroplastic deformation also has a natural explanation in the framework of the proposed model. Because electron–dislocation interaction weakly depends on moderate temperatures, electroplastic deformation of metals must show an equally weak temperature dependence. The above experiments constitute the first stage of research into metal electroplastic deformation. The authors of Ref. [51] predicted that a deeper insight into the influence of the electronic state of metals on their mechanical properties would promote elucidation of mechanisms of electron–dislocation interaction and radiative action of accelerated electrons or other charged particles. It can be supposed that extending such investigations to lower temperature ranges and higher current densities and frequencies with the use of high-frequency techniques for the study of crystals containing mobile dislocations under extreme irradiation conditions (e.g., for the formation of superdense concentration of free electrons) will bring discoveries of new phenomena.

The experiments were carried out with the use of zinc (99.998% Zn), lead (99.9995% Pb), indium (99.9995% In) single crystals, alloyed zinc (2×10^{-20}% Cd) with orientation in the center of a standard triangle, polycrystalline zinc, cadmium, tin, lead, and indium samples of at least 99.99% purity. Electric contacts welded at the ends of all specimens were connected with a source of current. Tensile and compressive tests at a constant rate of 0.1 mm min^{-1} were conducted using an Instron testing machine or a specially designed remote setup (in the case of irradiation experiments). The specimens were fastened with insulated clamps. Loads were measured to the nearest 2 g. Samples 15–16 mm in length and 1 mm in diameter were used in tensile and relaxation experiments. Compressive tests were performed with 6-mm long samples 2.5 mm in diameter.

In stress relaxation experiments, sample deformation was stopped after some time to record decreased elastic dynamometer readings attributable to plastic deformation of the specimens. Sample creep under the effect of applied constant stress with 25-g loading steps was tested using a remote setup with the testing section based on an E-2D1 mechanoelectronic transducer. Deformations were measured within a 0.2% accuracy. Creep time equaled 10 min.

Deformation within the first 3 s after the application of the load characterized the unsteady creep rate v_{cr}^{uns} of the sample. The average creep rate for the last 9 min of deformation was taken as the steady creep rate v_{cr}^{s}. In the case of exposure to electric current, a battery of 10^3 μF electrolytic capacitors was periodically discharged through strained samples at a rate of roughly 0.1 C per pulse, pulse duration of $\sim 10^{-4}$ s, pulse repetition rate of 0.3–0.4 Hz, and voltage of 50–200 V. At the liquid-nitrogen temperature, heat release under the effect of current pulses did not exceed 5–10 mW, and the samples were less than fractions of a degree warmer than in the absence of the treatment. The difference failed to be recorded by differential chromel–copel thermocouples welded to the specimens. The experimental regimes guaranteed the bulk effect of the current (the absence of the skin effect) and a small magnetostriction effect determined by the self-magnetic field of the sample (pinch effect).

A new physical phenomenon, the electroplastic effect, discovered in a series of experimental studies reported by O A Troitskii and co-workers [6, 51], consists in reduced deformation resistance and increased plasticity in metals under the influence of electric current, in addition to its thermal and ponderomotive action. The effect is characterized by the following features:

— Jumpwise plastic strain of metal crystals in current pulses, with the effect being especially pronounced in the sample's yield stress region; improved homogeneity of shear structures; enhancement of the effect in a surface-active medium; controllability of the process — dependence of jump magnitude on the current strength and pulse repetition rate; weak temperature dependence.

— Current pulses increase plastic deformation of amalgamated zinc crystals, preceding their brittle fracture, by 100–120 % at 78 K and 50–60% at room temperature. The critical level of normal stresses on the glide planes p increases in the process of electroplastic deformation, while the dependence of p on the specific crystallographic shift $a(\kappa)$ becomes weaker as a result of reduced brittle fracture. The current action lowers the critical cleavage stresses in the glide planes as a consequence of diminished starting stresses for dislocation movements. The metal cold-brittleness boundary shifts to the lower temperature region under the influence of the current.

— A rise in the pulse repetition rate heightens the effect, as estimated from altered crystal strain resistance. At the same time, the magnitude of individual jumps of deformation decreases as a result of exhaustion of dislocation structure under the effect of previous pulses. The frequency factor plays an important role in attempts to have dislocations overcoming obstacles in glide planes.

— A rise in current amplitude density in crystals enhances the effect, starting from certain threshold current densities. It takes some time for current-induced metal plastic deformation to develop, the delay ranging from a few to tens of seconds.

— Prolonged current pulses heighten the effect, which becomes apparent starting from certain threshold pulse lengths corresponding to elementary strain jump times in crystals. The dependence of the effect on the pulse length can be attributed to a change in the dislocation structure impulse in crystals.

— Research on the dependence of EPE on metal deformation conditions and the presence of impurities in metals revealed higher strain jumps with an increase in crystal stretch rate, which is associated with the accumulation of dislocation pileups and their stripping under the influence of the current. The effect is characterized by a weak temperature dependence. The current action increases with increasing impurity content in the metal up to 1 at.% due to improved homogeneity of shear structures formed in crystals and the influence of the current on the accumulation and disruption of incomplete shears. Simultaneously, alloying increases mechanical and electrical stress thresholds at which effects of the current action become apparent.

— Under special current passage conditions (paired pulses oriented either in the same or in opposite directions with different spacings between them) and electron acceleration of plastic flow, EPE can be attenuated, i.e., its partial inversion or metal plastic flow slow-down by the current can occur.

— A qualitative consideration of Fermi surface parameters revealed their important role in EPE enhancement in metals and the role of Fermi current carriers (electrons and holes) in energy and power momenta transfer into dislocations. Simultaneously, the role of Fermi surface closure, small volumes, and fragments, as well as favorable displacement directions and electric contact between the strained metal and another metal in this process were evaluated. Possible transformations of the Fermi surface and correlation of its state with the magnitude of EPE in face-centered cubic and hexagonal close-packed metals were analyzed, together with the mechanism of momenta transfer from current carriers to dislocations.

— An EPE model was proposed taking into account the basic premises of the dynamic and inertia theory of conduction electron involvement in metal plastic deformation on the assumption of equivalence of current action to application of additional effective stresses to crystals, the influence of current on dislocation pileups, and their rearrangement and breakaway from stoppers in the form of obstacles, impurities, and dislocations in other glide systems.

The authors of Ref. [6] summarized as follows the results of a theoretical consideration of electroplastic deformation (EPD) by A M Roshchupkin and I D Bataronov, who have explained the main experimental findings available at that time:

• The calculated function of screened electronic reaction of a metal in the current state allows analyzing changes in the energy of interaction between a dislocation and a local stopper in the presence of high-density current. For ordinary impurities, these changes can be significant only in electric fields of atomic scale.

• A microscopic theory of the dynamic pinch effect is constructed in the framework of the electron theory of metals, and the related effects of mechanical action on a strained metal are studied, including those of a polar character, even if the pinch effect itself is nonpolar by virtue of its quadratic dependence on the current.

• Various effects emerging during the formation of a nonuniform temperature field and the accompanying stresses in a conductor are analyzed. It is shown that the action of a current pulse gives rise to thermoelastic stresses of the same magnitude as those associated with the pinch effect.

• A general expression for the strength of electron–phonon entrainment of dislocations and point defects provides a basis for the analysis of contributions coming from phonon, electron, and electron–phonon entrainment mechanisms to the forces generated by thermal fluxes and electric current. The power action of the electric current on point defects and interfaces is shown to be underlain by the electron entrainment mechanism, whereas the electron–phonon entrainment force appears to be of greater importance for dislocations.

• A mechanism of dislocation pile-up breakaway from stoppers and the destruction of internal stress fields in metals under the influence of current pulses is proposed based on the dynamic properties of stopped dislocation pileups. The experimentally determined time of delay of the pulsed current action coincides with the dynamic reaction time of a dislocation pileup.

• Theoretical knowledge of metal plastic deformation processes under the influence of electric current remains incomplete and controversial, and the physical nature of metal plasticization effect awaits clarification.

The description of EPE and MPE below is based on the approach developed to describe the nonequilibrium electron–phonon subsystem of a crystal in electric and/or magnetic fields. Differentiation between contributions of magnetic and electric components of an alternating magnetic field to the influence on structural defects of a real crystal requires consideration of the microscopic models that constitute the subject matter of Section 6 [19, 33–37, 50].

6. Nonequilibrium kinetics of the crystal electron–phonon subsystem in an electric field as a basis of the electroplastic effect

The data presented in this section indicate that the observed EPE characteristics may serve as a quantitative description taking into consideration the influence on dislocation motion of nonequilibrium phonons excited by nonequilibrium electrons that received energy from an electric field. The EPE development scenario is shown as a flow chart in Fig. 17.

The plastic deformation of crystals under the exposure to external loads is in most cases mediated through dislocation glide. The basic equation describing the kinetics of the plastic deformation process is the modified Orovan equation (see, e.g., monograph [52]):

$$\dot{\varepsilon}_{\mathrm{d}} = bl\rho_{\mathrm{d}} v_{\mathrm{d}}(\sigma^*)\,, \qquad \sigma^* = \sigma - \sigma_{\mathrm{i}}\,, \tag{6.1}$$

where $\dot{\varepsilon}_{\mathrm{d}}$ is the strain rate, b is the Burgers vector, l is the average distance between stoppers, ρ_{d} is the mobile dislocation density, $v_{\mathrm{d}}(\sigma^*)$ is the frequency of overcoming barriers by dislocations, σ^* is the effective shear stress, and σ_{i} is the internal shearing stress in the glide plane.

6.1 Modification of Granato-Lücke model describing the influence of phonons on dislocation motion

In the case of thermodynamic equilibrium, the expression for $v_{\mathrm{d}}(\sigma^*, T)$ has the form

$$v_{\mathrm{d}}(\sigma^*, T) = v_{\mathrm{d}}^0 \exp\left(-\frac{H(\sigma^*)}{k_{\mathrm{B}}T}\right), \tag{6.2}$$

where k_{B} is the Boltzmann constant.

The explicit form of function $H(\sigma^*)$ depends on the potential barrier model. The Landau–Gofman model [53] is used to consider the more general case in which electron and phonon subsystems cannot be, generally speaking, in thermodynamic equilibrium. The potential well has a parabolic shape:

$$U(x) = \begin{cases} \zeta x^2\,, & |x| \leqslant x_{\mathrm{cr}}\,, \\ 0\,, & |x| > x_{\mathrm{cr}}\,, \end{cases} \qquad \zeta x_{\mathrm{cr}}^2 = U_0\,. \tag{6.3}$$

The displacement of the dislocation segment L under the effect of stress σ is described in the string elastic vibration

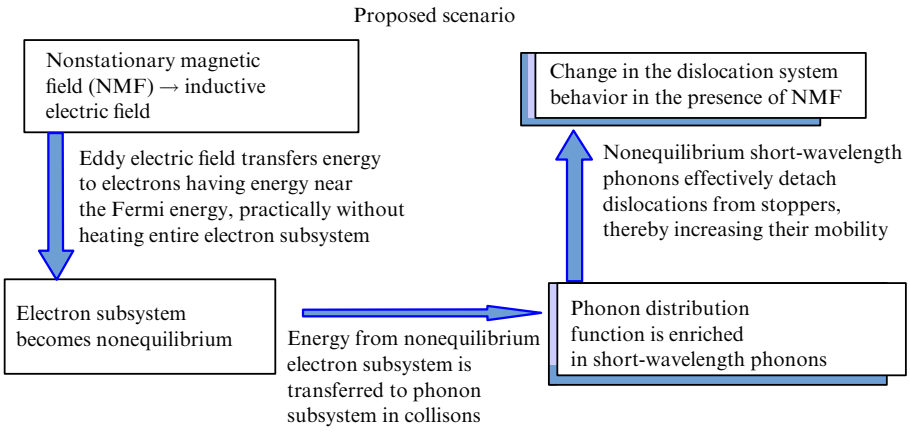

Figure 17. Proposed flow chart of EPE development.

approximation (Granato–Lücke model) [54]:

$$M\frac{\partial^2 u}{\partial t^2}+B\frac{\partial u}{\partial t}-C\frac{\partial^2 u}{\partial y^2}=b\sigma+f(t)\,. \tag{6.4}$$

Here, $u(y,t)$ is the displacement of the dislocation line at point y in direction x, $M=\rho b^2/2$ is the effective mass per unit length, ρ is the density of the material, B is the coefficient of dynamic friction force per unit length, $C=Gb^2/2$ is the string linear tension, G is the shear modulus, and $f(t)$ is the force of random pushes in the crystal per dislocation unit length. The boundary conditions are as follows:

$$u'(0,\,t)=ku(0,t)\,,\quad -u'(L,\,t)=ku(L,t)\,,\quad k=\frac{2\zeta}{C}\,. \tag{6.5}$$

Equation (6.4) being linear, its solution can be expressed as the sum

$$u(y,t)=u_{\rm st}(y)+u_{\rm osc}(y,t)\,,$$

where $u_{\rm st}(y)$ is the static deflection caused by external stress σ, $u_{\rm osc}(y,t)$ are the oscillations under the effect of random forces:

$$u_{\rm st}(y)=\frac{by(L-y)}{2C}+\frac{bL\sigma}{2Ck}\,, \tag{6.6a}$$

$$u_{\rm osc}(y,t)=\sum_{n=1}^{N}Q_n(t)\left(\sin(q_n y)+\frac{q_n}{k}\cos(q_n y)\right),$$

$$\cot(q_n y)=\frac{q_n^2-k^2}{2q_n k}\,. \tag{6.6b}$$

The quantity $Q_n(t)$ satisfies the following equation:

$$M\ddot{Q}_n(t)+B\dot{Q}_n(t)+M\omega_n^2 Q_n(t)=f_n(t)\,,\quad \omega_n^2=q_n^2\frac{C}{M}\,. \tag{6.7}$$

Let us consider the 'pinning point' at $y=0$. Suppose that fragment lengths on both its sides equal L. Then, the overall deviation at the 'pinning point' has the form

$$\tilde{u}(0,t)=2u_{\rm st}(y)+2u_{\rm osc}(y,t)=\tilde{u}_{\rm st}(y)+\tilde{u}_{\rm osc}(y,t)\,. \tag{6.8}$$

The random force situation was considered in Ref. [54]. Here are some calculations for indicative purposes. If a random event occurs at a certain moment, such that $\delta\tilde{u}(0,t)\geqslant\delta\tilde{u}_{\rm cr}$, the conditions for overcoming the obstacle will be satisfied. Let $f_n(t)$ be the stationary Gaussian process. Equation (6.7) being linear, $Q_n(t)$ and, accordingly, $\tilde{u}(0,t)$ are also stationary Gaussian processes for which the mean number of jumps higher than $\delta\tilde{u}_{\rm cr}$ per unit time is expressed as

$$\nu=\frac{1}{2\pi}\sqrt{-\frac{\Psi''(0)}{\Psi(0)}}\exp\left(-\frac{\delta\tilde{u}_{\rm cr}^2}{2\Psi(0)}\right), \tag{6.9}$$

$$\Psi(\tau)=2\sum_{n=1}^{\tilde{n}}\frac{q_n^2}{k^2}\,\overline{Q_n(t)Q_n(t+\tau)}\equiv\sum_{n=1}^{\tilde{n}}\frac{q_n^2}{k^2}\,\psi(\tau)\,, \tag{6.10}$$

$$\delta\tilde{u}_{\rm cr}=x_{\rm cr}-\frac{bL\sigma}{Ck}=x_{\rm cr}\left(1-\frac{\sigma}{\sigma_{\rm cr}}\right),\quad \sigma_{\rm cr}\equiv\frac{Ckx_{\rm cr}}{bL}\,, \tag{6.11}$$

where $\Psi(\tau)$ is the correlation function of the random process $\delta\tilde{u}(0,t)$, expressed through the correlation function $\psi(\tau)$ of the random process $Q_n(t)$, and $\Psi''(0)$ is the second derivative in τ at $\tau=0$. For the Fourier component $Q_{n\omega}$ of $Q_n(t)$, one has

$$\psi(\tau)=\int_{-\infty}^{\infty}Q_{n\omega}^2\exp(-{\rm i}\omega\tau)\,{\rm d}\omega\,, \tag{6.12}$$

where $Q_{n\omega}^2$ is defined by the relation

$$\overline{Q_{n\omega}Q_{n\omega'}}=Q_{n\omega}^2\delta(\omega+\omega')\,. \tag{6.13}$$

Each of these quantities can be formally regarded as an independent oscillator with friction χ and harmonic frequency ω_n:

$$m\ddot{Q}+\chi\dot{Q}+m\omega_n^2 Q=F\,, \tag{6.14}$$

where m is the coefficient of proportionality between the generalized momentum and the velocity $\dot{Q}$, χ is the coefficient of friction, and F is a random force [53–55]:

$$m=M\frac{L\xi_n}{2}\,,\quad \chi=B\frac{L\xi_n}{2}\,,\quad F=f_n\frac{L\xi_n}{2}\,,$$
$$\xi_n=1-\frac{2}{kL}+\frac{q_n^2}{k^2}\,. \tag{6.15}$$

In this way, the following formula can be obtained for the Fourier component:

$$Q_{n\omega}^2=\frac{F_\omega^2}{m^2(\omega_n^2-\omega^2)^2+\chi^2\omega^2}\,. \tag{6.16}$$

The spectral density of the random force can be found from the expression [19, 36, 37]

$$F_\omega^2=\frac{\chi}{\pi}\hbar\omega\left(\frac{1}{2}+N(\omega)\right). \tag{6.17}$$

Therefore, the phonon distribution function $N(\omega)$ needs to be found first to evaluate the force acting on dislocations from phonons.

6.2 Kinetic equations for electron and phonon distribution functions

Certain studies on electron–phonon subsystem dynamics in metallic films were based on the assumption of the Fermi–Dirac form of the isotropic part of the electron distribution function having a time-dependent temperature [56]. In this review, we put aside this assumption following our previous publications [19, 33–37]; therefore, the calculated distribution functions can, as a matter of fact, be strongly nonequilibrium. In this case, the electron and phonon behavior is described by distribution functions.

To describe nonequilibrium dynamics of the electron–phonon subsystem, a system of Boltzmann kinetic equations needs to be solved for electron and phonon distribution functions $f(\mathbf{r},\mathbf{p},t)$ and $N(\mathbf{r},\mathbf{p},t)$, respectively. The Boltzmann kinetic equation for the electron distribution function has the form

$$\frac{\partial f}{\partial t}+\mathbf{v}\,\frac{\partial f}{\partial\mathbf{r}}+\frac{\partial f}{\partial\mathbf{p}}\,\frac{{\rm d}\mathbf{p}}{{\rm d}t}=I_{\rm ee}+I_{\rm ep}+I_{\rm ed}\,, \tag{6.18}$$

$$\frac{{\rm d}\mathbf{p}}{{\rm d}t}=e\Big(\mathbf{E}(\mathbf{r},t)+\big[\mathbf{v},\mathbf{B}(\mathbf{r},t)\big]\Big)\,, \tag{6.19}$$

where $\mathbf{v}$ is the velocity, $\mathbf{p}$ is the momentum, t is the time, $\mathbf{r}$ is the radius vector, $\mathbf{E}$ is the electric field strength, and $\mathbf{B}$ is the magnetic induction.

In what follows, we shall consider situations in which parameters of the magnetic field are such that its nonstationarity is essential and accounts for the appearance of an eddy induction electric field, whereas the influence of the magnetic field on the curving of electron paths is unessential, which makes it possible to ignore the second item on the right-hand side of equation (6.19). For simplicity, the electric field and electron and phonon distribution functions are assumed to be spatially uniform.

In general, *the electron–electron collision integral* I_{ee} has the following form for conductors and semiconductors with degenerate electron gas [57–59]:

$$I_{ee} = \frac{2}{(2\pi\hbar)^6}\int \mathrm{d}\mathbf{p}_1\,\mathrm{d}\mathbf{p}_2\,\mathrm{d}\mathbf{p}_3 W(\mathbf{p},\,\mathbf{p}_1|\,\mathbf{p}_2,\,\mathbf{p}_3)\big[f(\mathbf{p}_2,t)f(\mathbf{p}_3,t) \times \big(1-f(\mathbf{p}_1,t)\big)\big(1-f(\mathbf{p},t)\big) - f(\mathbf{p},t)f(\mathbf{p}_1,t) \times \big(1-f(\mathbf{p}_2,t)\big)\big(1-f(\mathbf{p}_3,t)\big)\big]\,\delta(\varepsilon+\varepsilon_1-\varepsilon_2-\varepsilon_3) \times \delta(\mathbf{p}+\mathbf{p}_1-\mathbf{p}_2-\mathbf{p}_3)\,, \tag{6.20}$$

where $f(\mathbf{p},\,t)$ is the spatially uniform electron distribution function (occupation numbers), $\varepsilon_i = \varepsilon(\mathbf{p}_i)$ is the energy of an electron with momentum $\mathbf{p}_i$, $W(\mathbf{p},\,\mathbf{p}_1|\,\mathbf{p}_2,\,\mathbf{p}_3)$ is the matrix element describing the screened Coulomb interaction (see, e.g., Refs [57–59] for the 'jelly' model):

$$W(\mathbf{p},\,\mathbf{p}_1|\,\mathbf{p}_2,\,\mathbf{p}_3) = (2\pi\hbar)^3 2e^4\big(|\,\mathbf{p}_1-\mathbf{p}_3|^2+a_1^2\big)^{-2}\,, \tag{6.21}$$

here $W(\mathbf{p},\,\mathbf{p}_1|\,\mathbf{p}_2,\,\mathbf{p}_3)$ is the probability of scattering of electrons with $\mathbf{p}_2$ and $\mathbf{p}_3$ momenta into the states with $\mathbf{p}$ and $\mathbf{p}_1$ momenta as a result of collision, and a_1 is the characteristic screening parameter. For relatively low electric field strengths, the contribution of electron–electron collisions to the formation of the isotropic part of the electron distribution function is significantly smaller than the contribution from electron–phonon interactions. Therefore, in what follows, the electron–electron collisions at small time intervals will not be taken into consideration.

The electron–phonon collision integral I_{ep} [57–59] takes the form

$$I_{ep} = \int \mathrm{d}\mathbf{q}\,w(\mathbf{q})\Big\{\delta\big(\varepsilon(\mathbf{p}+\mathbf{q})-\varepsilon(\mathbf{p})-\hbar\Omega(\mathbf{q})\big) \times \big[f(\mathbf{p}+\mathbf{q},t)\big(1-f(\mathbf{p},t)\big)\big(N(\mathbf{q},t)+1\big) - f(\mathbf{p},t)\big(1-f(\mathbf{p}+\mathbf{q},t)\big)N(\mathbf{q},t)\big] + \delta\big(\varepsilon(\mathbf{p}-\mathbf{q})-\varepsilon(\mathbf{p})+\hbar\Omega(\mathbf{q})\big) \times \big[f(\mathbf{p}-\mathbf{q},t)\big(1-f(\mathbf{p},t)\big)N(\mathbf{q},t) - f(\mathbf{p},t)\big(1-f(\mathbf{p}-\mathbf{q},t)\big)\big(N(\mathbf{q},t)+1\big)\big]\Big\}\,, \tag{6.22}$$

where $N(\mathbf{q},t)$ is the spatially uniform phonon distribution function. (For simplicity, we do not explicitly write out the time dependences of electron and phonon distribution functions.)

Electron-impurity or *electron-defect collision integrals* I_{ed} can be obtained by substituting $\hbar\Omega = 0$ and $N(\mathbf{q},\,t) = 0$ into I_{ep}:

$$I_{ed} = \int \mathrm{d}\mathbf{p}'\,w_{ed}(\mathbf{p}'-\mathbf{p})\delta\big(\varepsilon(\mathbf{p}')-\varepsilon(\mathbf{p})\big)\big(f(\mathbf{p}')-f(\mathbf{p})\big)\,. \tag{6.23}$$

The phonon distribution function also satisfies the kinetic equation

$$\frac{\partial N(\mathbf{q})}{\partial t} = I_{pe} + I_{pp} + I_{pd}\,. \tag{6.24}$$

The *phonon–electron collision integral* I_{pe} [57–59] has the form

$$I_{pe} = \int \mathrm{d}\mathbf{p}\,w(\mathbf{q})\Big\{\delta\big(\varepsilon(\mathbf{p}+\mathbf{q})-\varepsilon(\mathbf{p})-\hbar\Omega(\mathbf{q})\big)\big[f(\mathbf{p}+\mathbf{q}) \times \big(1-f(\mathbf{p})\big)\big(N(\mathbf{q})+1\big)\big] - f(\mathbf{p})\big(1-f(\mathbf{p}+\mathbf{q})\big)N(\mathbf{q})\Big\}\,. \tag{6.25}$$

Phonon–phonon (I_{pp}) and phonon–defect (I_{pd}) collision integrals are expressed in the τ-approximation as

$$I_{pp} = -\nu_{pp}(\mathbf{q})\big[N(\mathbf{q})-N_T(\mathbf{q})\big]\,,\quad \nu_{pp}(\mathbf{q}) = \nu_{pp0}q^2\,, \qquad \nu_{pp0} = \frac{T^3 s}{a_c T_D^4 M_c}\,, \tag{6.26}$$

$$I_{pd} = -\nu_{pd}(\mathbf{q})\big[N(\mathbf{q})-\overline{N(\mathbf{q})}\big]\,, \tag{6.27}$$

where $N_T(q) = [\exp(\hbar\Omega/T)-1]^{-1}$ is the thermodynamically equilibrium phonon distribution function, i.e., the Bose–Einstein function, and $\overline{N(q)} = (1/4\pi)\int N(\mathbf{q})\,\mathrm{d}o$ is the phonon distribution function averaged over angles.

We shall assume that electron–impurity and electron–defect collisions are responsible for isotropization of the electron distribution function, and seek it in the form of the sum of an isotropic distribution function and a small anisotropic addition:

$$f(\mathbf{p}) = f(\varepsilon(p)) + \mathbf{f}_1\big(\varepsilon(p)\big)\,\frac{\mathbf{p}}{p}\,, \tag{6.28}$$

$$w(q) = w_0 q\,,\quad w_0 = \frac{\varepsilon_{1A}^2}{2(2\pi\hbar)^2\hbar\rho s}\,,\quad \hbar\Omega(q) = sq\,, \tag{6.29}$$

where s is the speed of sound, ρ is the density of the material, ε_{1A} is the deformation potential constant equaling $2\varepsilon_F/3$ in our concrete model, and ε_F is the Fermi energy.

Concretization and substitution of parameters yield

$$I_{pp} = -\nu_{pd0}q\big[N(\mathbf{q})-N_T(\mathbf{q})\big]\,, \tag{6.30}$$

$$I_{ed}\left\{\mathbf{f}_1(\varepsilon)\,\frac{\mathbf{p}}{p}\right\} = -\nu_{ed}\,\mathbf{f}_1(\varepsilon)\,\frac{\mathbf{p}}{p}\,, \tag{6.31}$$

where $\nu_{ed} = 3\times10^{13}\ \mathrm{s}^{-1}$ is the frequency of electron–impurity/defect collisions that in this case (low temperatures) determines isotropization of the electron distribution function:

$$I_{ep}\left\{\mathbf{f}_1(\varepsilon)\,\frac{\mathbf{p}}{p}\right\} = -\nu(\varepsilon)\,\mathbf{f}_1(\varepsilon)\,\frac{\mathbf{p}}{p}\,, \qquad \nu(\varepsilon) = \frac{\pi w_0}{\sqrt{m\varepsilon^3}}\int_0^{\sqrt{8m\varepsilon}} q^3\left(N(q)+\frac{1}{2}\right)\mathrm{d}q\,. \tag{6.32}$$

For the anisotropic addition, one has

$$\frac{\partial \mathbf{f}_1}{\partial t}\,\frac{\mathbf{p}}{p} - e\mathbf{E}\mathbf{v}\frac{\partial f_0}{\partial\varepsilon} = -\nu_{ed}\,\mathbf{f}_1(\varepsilon)\,\frac{\mathbf{p}}{p}\,. \tag{6.33}$$

Electron collisions with defects and impurities in real polycrystalline specimens occur very frequently, at a time scale that is small compared with the characteristic time of phonon-electron interactions; therefore, the anisotropic addition can be regarded as stationary and spatially uniform.

As a result, here is the final system of two equations for isotropic electron and acoustic phonon distribution functions [33–36] that will be solved without expanding the electron distribution function in a Taylor series:

$$\frac{\partial f}{\partial \tilde{t}} - 4\Delta\tilde{\varepsilon}\,\frac{1}{\tilde{\varepsilon}^{1/2}}\,\frac{\partial}{\partial\tilde{\varepsilon}}\left(\tilde{\varepsilon}^{3/2}\frac{\partial f}{\partial\tilde{\varepsilon}}\right)$$
$$= \frac{1}{8}\alpha^{-5/2}\left\{\frac{1}{\sqrt{\tilde{\varepsilon}}}\int_0^{\varepsilon_-} \mathrm{d}\tilde{\varepsilon}_{\mathrm{ph}}\,\tilde{\varepsilon}_{\mathrm{ph}}^2\Big[f(\tilde{\varepsilon}-\tilde{\varepsilon}_{\mathrm{ph}})N(\tilde{\varepsilon}_{\mathrm{ph}})$$
$$+ f(\tilde{\varepsilon})\big(f(\tilde{\varepsilon}-\tilde{\varepsilon}_{\mathrm{ph}}) - 1 - N(\tilde{\varepsilon}_{\mathrm{ph}})\big)\Big]$$
$$+ \frac{1}{\sqrt{\tilde{\varepsilon}}}\int_0^{\varepsilon_+} \mathrm{d}\tilde{\varepsilon}_{\mathrm{ph}}\,\tilde{\varepsilon}_{\mathrm{ph}}^2\Big[f(\tilde{\varepsilon}+\tilde{\varepsilon}_{\mathrm{ph}})\big(N(\tilde{\varepsilon}_{\mathrm{ph}})+1\big)$$
$$- f(\tilde{\varepsilon})\big(f(\tilde{\varepsilon}+\tilde{\varepsilon}_{\mathrm{ph}}) + N(\tilde{\varepsilon}_{\mathrm{ph}})\big)\Big]\Big\}, \tag{6.34}$$

$$\frac{\partial N(q)}{\partial\tilde{t}} = \frac{1}{2\alpha}\int_{\varepsilon_0}^{\infty}\mathrm{d}\tilde{\varepsilon}\,\Big[\big(f(\tilde{\varepsilon}+\tilde{\varepsilon}_{\mathrm{ph}}) - f(\tilde{\varepsilon})\big)N(\tilde{\varepsilon}_{\mathrm{ph}})$$
$$+ f(\tilde{\varepsilon}+\tilde{\varepsilon}_{\mathrm{ph}})\big(1-f(\tilde{\varepsilon})\big)\Big]. \tag{6.35}$$

The following notations were introduced here:

$$\alpha = \frac{ms^2}{2k_{\mathrm{B}}T_{\mathrm{e}}}, \qquad \Delta\tilde{\varepsilon} = \frac{e^2E^2\tau_{\mathrm{ep0}}}{6mv_{\mathrm{ed}}\,k_{\mathrm{B}}T_{\mathrm{e}}}, \qquad \tilde{\varepsilon} = \frac{\varepsilon}{k_{\mathrm{B}}T_{\mathrm{e}}},$$
$$\tilde{p} = \frac{p}{\sqrt{2mk_{\mathrm{B}}T_{\mathrm{e}}}}, \qquad \tilde{\varepsilon}_{\mathrm{ph}} = \frac{\varepsilon_{\mathrm{ph}}}{k_{\mathrm{B}}T_{\mathrm{e}}}, \qquad \tilde{t} = \frac{t}{\tau_{\mathrm{ep0}}},$$
$$\tilde{q} = \frac{q}{\sqrt{2mk_{\mathrm{B}}T_{\mathrm{e}}}}, \qquad \tau_{\mathrm{ep0}} = \frac{(2\pi\hbar)^3\hbar\rho}{\pi m^3 s\varepsilon_{1A}^2} = 3{,}446\times10^{-7}\ \mathrm{s}.$$

The integration limits deduced from the laws of momentum and energy conservation have the respective forms

$$\varepsilon_- = \min\left[4\big(\sqrt{\tilde{\varepsilon}\alpha}-\alpha\big),\,\tilde{\varepsilon}_{\mathrm{ph}}^{\mathrm{D}}\right], \quad \varepsilon_+ = \min\left[4\big(\sqrt{\tilde{\varepsilon}\alpha}+\alpha\big),\,\tilde{\varepsilon}_{\mathrm{ph}}^{\mathrm{D}}\right],$$
$$\varepsilon_0 = \frac{\tilde{\varepsilon}_{\mathrm{ph}}^2}{16\alpha} - \frac{\tilde{\varepsilon}_{\mathrm{ph}}}{2} + \alpha, \tag{6.36}$$

where superscript D corresponds to the Debye phonon.

Electron ($f(\varepsilon)$) and phonon ($N(q)$) distribution functions are dimensionless quantities satisfying the following normalization conditions:

$$\frac{1}{2\pi^2}\left(\frac{2m}{\hbar^2}\right)^{3/2}\int_0^{\infty}\varepsilon^{1/2}f(\varepsilon)\,\mathrm{d}\varepsilon = n, \tag{6.37}$$

where n is the electron concentration in the valence band (for metals, the conduction band is filled only partially), and

$$\frac{1}{2\pi^2}\left(\frac{1}{\hbar^3}\right)\int_0^{q_{\mathrm{D}}} q^2N(q)\,\mathrm{d}q < \infty, \tag{6.38}$$

where q_{D} is the Debye phonon momentum defined as

$$q_{\mathrm{D}} = \frac{\pi\hbar}{a}. \tag{6.39}$$

All the values are taken for nickel: $s = 2.96\times10^3$ m s^{-1} is the transverse speed of sound, $n = 2.5\times10^{22}$ cm^{-3} is the concentration of conduction electrons, $a = 3.5\times10^{-8}$ is the lattice parameter, and conductivity $\rho_{\mathrm{s}}^{-1} = 0.333\times10^6$ S cm^{-1}.

The thermodynamically equilibrium electron-energy distribution function is the Fermi–Dirac function:

$$f_0(\varepsilon) = \left[\exp\left(\frac{\varepsilon-\varepsilon_{\mathrm{F}}}{k_{\mathrm{B}}T_{\mathrm{e}}}\right)+1\right]^{-1}. \tag{6.40}$$

For nickel, $\varepsilon_{\mathrm{F}} = 5\times10^{-19}$ J.

6.3 Numerical solution to a system of kinetic equations for electron and phonon distribution functions and a discussion of results

For the numerical solution of a system of kinetic equations (6.34), (6.35), the finite difference method of the first-order approximations over time, and second-order in the energy space was used. The (6.34), (6.35) system was reduced to a system of difference equations [36]:

$$\frac{f_i^{\nu+1}-f_i^{\nu}}{\tilde{\tau}} = 6\Delta\tilde{\varepsilon}\,\frac{f_{i+1}^{\nu+1}-f_{i-1}^{\nu+1}}{2h_{\tilde{\varepsilon}}}$$
$$+ 4\tilde{\varepsilon}_i\Delta\tilde{\varepsilon}\,\frac{f_{i+1}^{\nu+1}-2f_i^{\nu+1}+f_{i-1}^{\nu+1}}{h_{\tilde{\varepsilon}}^2} + J_i, \tag{6.41}$$

$$J_i = \frac{1}{8\sqrt{\tilde{\varepsilon}_i\alpha^5}}\,\frac{1}{2}\left\{\sum_{j=0}h_{\tilde{\varepsilon}_{\mathrm{ph}}}\tilde{\varepsilon}_{\mathrm{ph}_j}^2\big[f_k^{\nu}N_j + f_i^{\nu}(f_k^{\nu}-N_j-1)\big]\right.$$
$$+\sum_{j=0}h_{\tilde{\varepsilon}_{\mathrm{ph}}}\tilde{\varepsilon}_{\mathrm{ph}_j}^2\big[f_l^{\nu}(N_j+1) - f_i^{\nu}(f_l^{\nu}+N_j)\big]$$
$$+\sum_{j=0}h_{\tilde{\varepsilon}_{\mathrm{ph}}}\tilde{\varepsilon}_{\mathrm{ph}_{j+1}}^2\big[f_{k-1}^{\nu}N_{j+1} + f_i^{\nu}(f_{k-1}^{\nu}-N_{j+1}-1)\big]$$
$$\left.+\sum_{j=0}h_{\tilde{\varepsilon}_{\mathrm{ph}}}\tilde{\varepsilon}_{\mathrm{ph}_{j+1}}^2\big[f_{l+1}^{\nu}(N_{j+1}+1) - f_i^{\nu}(f_{l+1}^{\nu}+N_{j+1})\big]\right\}, \tag{6.42}$$

$$\frac{N_j^{\nu+1}-N_j^{\nu}}{\tilde{\tau}} = \frac{1}{2\alpha}\,\frac{1}{2}\sum_i h_{\tilde{\varepsilon}}\big[(f_l^{\nu}-f_i^{\nu})N_j^{\nu} + f_l^{\nu}(1-f_i^{\nu})$$
$$+ (f_{l+1}^{\nu}-f_{i+1}^{\nu})N_j^{\nu} + f_{l+1}^{\nu}(1-f_{i+1}^{\nu})\big], \tag{6.43}$$

$$f_k^{\nu} = f(\tilde{\varepsilon}_i - \tilde{\varepsilon}_{\mathrm{ph}_j}), \qquad f_l^{\nu} = f(\tilde{\varepsilon}_i + \tilde{\varepsilon}_{\mathrm{ph}_j}),$$
$$f_{k-1}^{\nu} = f(\tilde{\varepsilon}_i - \tilde{\varepsilon}_{\mathrm{ph}_{j+1}}), \qquad f_{l+1}^{\nu} = f(\tilde{\varepsilon}_i + \tilde{\varepsilon}_{\mathrm{ph}_{j+1}}). \tag{6.44}$$

The summation limits were found from relations (6.36). Grid steps $\tilde{\varepsilon}_i$ were chosen such that the following equalities hold:

$$\tilde{\varepsilon}_i - \tilde{\varepsilon}_{\mathrm{ph}_j} = \tilde{\varepsilon}_k, \qquad \tilde{\varepsilon}_i + \tilde{\varepsilon}_{\mathrm{ph}_j} = \tilde{\varepsilon}_l, \tag{6.45}$$

where k and l are natural numbers. Calculations yielded electron and phonon distribution functions.

Figure 18a presents the dependence of the electron distribution function decimal logarithm $\log_{10}f(\varepsilon)$ on the dimensionless electron momentum $\tilde{p} = p/(2mk_{\mathrm{B}}T_{\mathrm{e}})^{1/2}$ at two electric field strengths, 5 and 10 V cm^{-1}, for different time instants (with a step of 50 ns) indicated in the captions to the figures. Figures 18b, d plot the dependence of the phonon distribution function $N(q)$ multiplied by $\tilde{q}^3$ on the dimensionless phonon momentum $\tilde{q} = q/(2mk_{\mathrm{B}}T_{\mathrm{e}})^{1/2}$ at two electric field strengths, 10 and 5 V cm^{-1}, for different time instants (with a step of 50 ns) indicated in the captions to the figures. It can be seen that the number of high-energy electrons and phonons grows monotonically with time. The curves for $t = 0$ (the lowest ones) correspond to equilibrium distribution functions. Specifically, the phonon distribution function multiplied by $\tilde{q}^3$ at the electric field strength 10 V cm^{-1} at

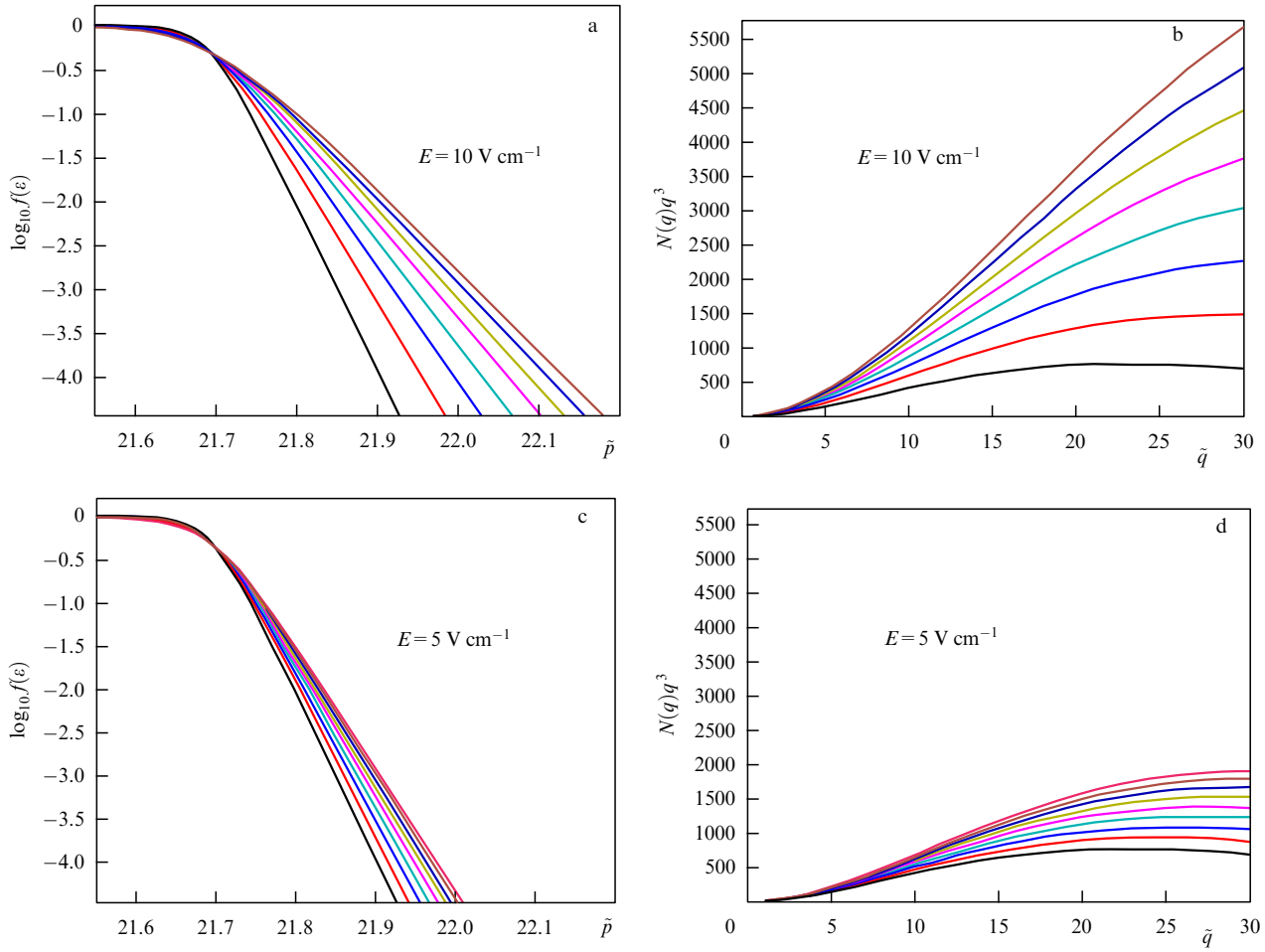

Figure 18. (a) Dependence of the electron distribution function decimal logarithm on the dimensionless electron momentum $\tilde{p}$ at $E = 10$ V cm^{-1} for different time instants $t = 0$, 50, 100, 150, 200, 250, 300, 350 ns. (b) Dependence of the phonon distribution function, multiplied by the dimensionless phonon momentum cubed $\tilde{q}^3$, on $\tilde{q}$ at $E = 10$ V cm^{-1} for $t = 0$, 50, 100, 150, 200, 250, 300, 350 ns. (c) Dependence of the electron distribution function decimal logarithm on $\tilde{p}$ at $E = 5$ V cm^{-1} for $t = 0$, 50, 100, 150, 200, 250, 300, 350 ns. (d) Dependence of the phonon distribution function, multiplied by $\tilde{q}^3$, on $\tilde{q}$ at $E = 5$ V cm^{-1} for $t = 0$, 50, 100, 150, 200, 250, 300, 350, 400 ns.

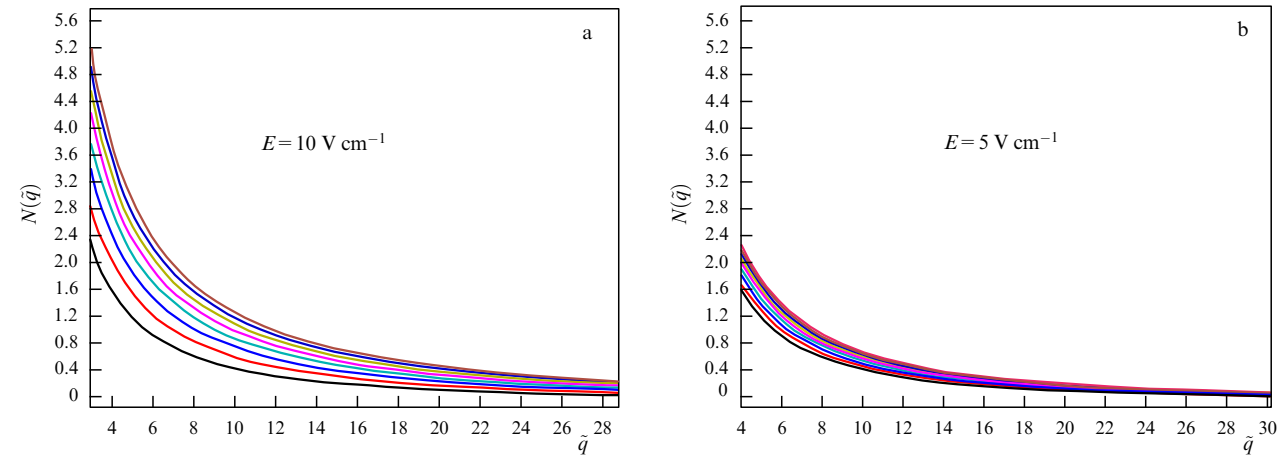

Figure 19. Dependence of the phonon distribution function on the dimensionless phonon momentum $\tilde{q}$ at the electric field strengths (a) $E = 10$ V cm^{-1} for $t = 0$, 50, 100, 150, 200, 250, 300, 350 ns, and (b) $E = 5$ V cm^{-1} for different time instants $t = 0$, 50, 100, 150, 200, 250, 300, 350, 400 ns.

the instant $t = 400$ ns is thrice that at 5 V cm^{-1} for the same time instant. For the same t and the electric field strength 5 V cm^{-1}, the electron momenta at which the electron distribution function is 10^{-4} differ by 1.00239 times, For the same t and the electric field strength 10 V cm^{-1}, the electron momenta at which the electron distribution function equals 10^{-4} differ by 1.00811 times. Figure 19 presents the dependence of the phonon distribution function decimal

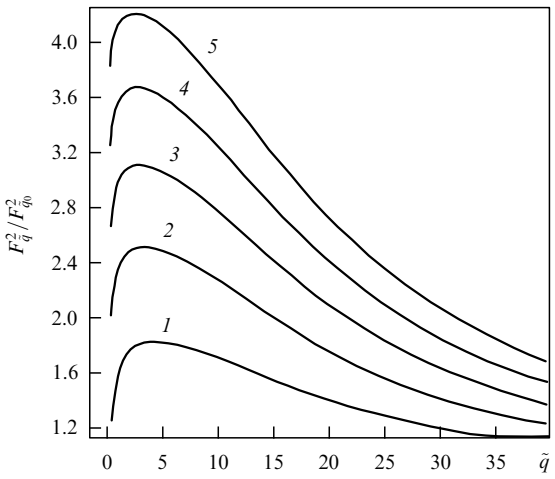

Figure 20. Dependence of the $F_{\tilde{q}}^2/F_{\tilde{q}_0}^2$ ratio on the dimensionless phonon momentum for different instants of time: $t = 0.25$ μs (curve *1*), 0.50 μs (curve *2*), 0.75 μs (curve *3*), 1.00 μs (curve *4*), and 1.25 μs (curve *5*) at $E = 10$ V cm^{-1}.

logarithm on the dimensionless phonon momentum $\tilde{q}$ for different time instants t at two values 10 and 5 V cm^{-1} of the electric field strength.

To evaluate the influence on plastic deformation, the following dependence was constructed (Fig. 20):

$$\frac{F_{\tilde{q}}^2}{F_{\tilde{q}_0}^2} = \frac{1/2 + N(\tilde{q})}{1/2 + N_0(\tilde{q})}\,, \tag{6.46}$$

where $N_0(\tilde{q})$ is the Bose–Einstein function at a temperature of 32 K, i.e., 12 K higher than the initial temperature, $N(\tilde{q})$ is the phonon distribution function found by numerical calculations, and $F_{\tilde{q}}$ is the random force spectral density [see formula (6.17)]. In most experiments [5], heating did not exceed 0.5–3 K.

Figure 20 shows that the force acting on dislocations from phonons is greater than in the case of simple heating and tends to increase with time.

6.4 Theoretical research on nickel softening under the creep regime in an alternating magnetic field

Because we study the behavior of a specimen in a harmonic and detected (monopolar) magnetic field, it is important to evaluate the influence of the eddy electric field induced by a nonstationary magnetic field on the change in the sample's mechanical properties. The characteristic strength of the electric field can be determined with the use of Maxwell equations:

$$\operatorname{rot}\mathbf{E} = -\frac{\partial}{\partial t}(\mu\mu_0\mathbf{H})\,, \quad E_0 = \frac{4\pi\mu_0 H_0}{\tau}\, l_x\left(\mu + H_z\,\frac{\partial\mu}{\partial H_z}\right), \tag{6.47}$$

$$H_z = H_0\left|\sin\frac{\pi t}{2\tau}\right|, \quad \mu = \mu\big(H_z(t), t\big)\,, \quad \mu_0 = 4\pi\times 10^{-7}\ \text{H m}^{-1},$$

where τ is the magnetic field growth time, and l_x is the sample width ($l_x = 3$ mm). As far as parameters of the experiment with harmonic monopolar pulses (see Section 4) are concerned, the sample width l_x is much greater than the thickness $l_y = 0.3$ mm, and the inductive electric field strength approaches 1 V cm^{-1}.

Moreover, the maximum contribution coming from longitudinal magnetostriction usually taken into account was estimated in Ref. [55]. Magnetostriction deformation can be disregarded because (1) it has the opposite sign and therefore has no effect on sample elongation, and (2) it does not exceed 10^{-4} of the observed experimental data.

For simplicity, we consider a spatially uniform electric field, as well as electron and acoustic phonon distribution functions when integrating the set of kinetic equations. The electron distribution function becomes isotropic due to electron–impurity collisions [36]. In our case, umklapp processes can be ignored, too. For relatively weak electric fields, the contribution of electron–electron collisions is much smaller than that from electron–phonon interactions; therefore, the former were not taken into account within the considered short time intervals.

For the phonon distribution function, we also took into consideration the finite lifetime of phonons in our system of kinetic equations

$$\frac{\partial N(\mathbf{q})}{\partial t} = I_{\text{pe}} - \frac{N_0(\mathbf{q}) - N(\mathbf{q})}{\tau_{\text{b}}} \tag{6.48}$$

[the second item on the right-hand side of formula (6.48)]. Here, I_{pe} is the phonon–electron collision integral [57–59], $N_0(\mathbf{q}) = \{\exp[\hbar\Omega/(k_{\text{B}}T_0)] - 1\}^{-1}$ is the thermodynamically equilibrium phonon distribution function — the Bose–Einstein function at T_0, $T_0 = 77$ K is the liquid-nitrogen temperature, $\hbar\Omega(q) = sq$, $\mathbf{q}$ is the phonon momentum, s is the transverse speed of sound, $\tau_{\text{b}} = (s/s_{\text{sub}})^2 l_y/2s$, and s_{sub} is the transverse sound speed in the substrate.

In the case being considered, the electron–phonon collision frequency is much lower than the electron–defect collision frequency. Collisions with defects and impurities occur very frequently, i.e., on a time scale smaller than the characteristic time of the interaction between phonons and electrons; therefore, the anisotropic addition can be regarded as stationary and spatially uniform.

As a result, there is a final set of two equations for the isotropic electron distribution and transverse acoustic phonon functions (6.34), (6.35) [19, 33–37] solved without applying the Taylor series expansion of the electron distribution function.

The thermodynamically equilibrium electron energy distribution function is the Fermi–Dirac function:

$$f_0(\varepsilon) = \left[\exp\left(\frac{\varepsilon - \varepsilon_{\text{F}}}{k_{\text{B}}T_{\text{e}}}\right) + 1\right]^{-1}, \tag{6.49}$$

where T_{e} is the initial electron temperature (77 K).

6.5 Comparison of theoretical and experimental data

Figure 21 shows the current density dependence of the drop of load. The drop was determined as follows. First, we substituted the values of the phonon distribution function into formula (6.17) and found the random force spectral density. Then, this expression was substituted into (6.16) to find

$$Q_{n\omega}^2 = \frac{(\chi/\pi)\hbar\omega[(1/2) + N(\omega)]}{m^2(\omega_n^2 - \omega^2)^2 + \chi^2\omega^2}\,. \tag{6.50}$$

The known $Q_{n\omega}^2$ value allowed the correlation function $\psi(0)$ and its second derivative to be calculated using formula

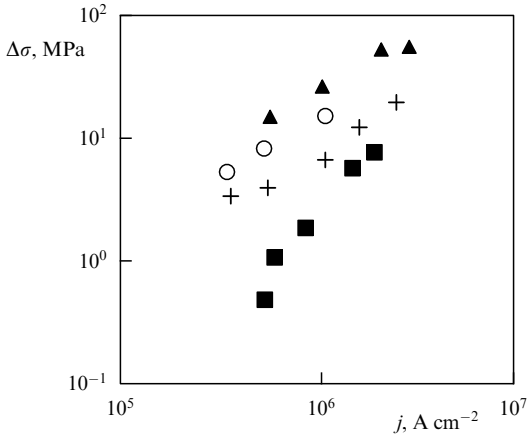

Figure 21. Dependence of the drop of load $\Delta\sigma$ on current density j. Squares denote experimental data obtained by O A Troitskii [5, 6, 51] for Ni; crosses are our results [36, 50, 60, 61] based on the modified Granato–Lücke and Landau–Gofman models with the phonon distribution function at the instant of time $t = 4$ μs for 1, 2, 5, 8, and 10 V cm^{-1} electric fields; circles show results for 1, 2, and 5 V cm^{-1} electric fields at $t = 12$ μs; triangles stand for results of experiments by V P Lebedev and S V Savich [62] for Cu.

(6.12):

$$\psi\big(0, N(\omega)\big) = \lim_{\tau\to 0}\int_{-\infty}^{\infty} \frac{(\chi/\pi)\hbar\omega\big[(1/2) + N(\omega)\big]}{m^2(\omega_n^2 - \omega^2)^2 + \chi^2\omega^2}\exp(-\mathrm{i}\omega\tau)\,\mathrm{d}\omega\,, \tag{6.51}$$

$$\psi''\big(0, N(\omega)\big) = -\lim_{\tau\to 0}\int_{-\infty}^{\infty} \frac{(\chi/\pi)\hbar\omega^3\big[(1/2) + N(\omega)\big]}{m^2(\omega_n^2 - \omega^2)^2 + \chi^2\omega^2}\exp(-\mathrm{i}\omega\tau)\,\mathrm{d}\omega\,.$$

Then, $\Psi(0)$ and $\Psi''(0)$ were found from formula (6.10):

$$\Psi\big(0, N(\omega)\big) = 2\sum_{n=1}^{\tilde{n}}\frac{q_n^2}{k^2}\,\psi\big(0, N(\omega)\big)\,, \tag{6.52}$$

$$\Psi''\big(0, N(\omega)\big) = 2\sum_{n=1}^{\tilde{n}}\frac{q_n^2}{k^2}\,\psi''\big(0, N(\omega)\big)\,. \tag{6.53}$$

Substituting formula (6.9) into (6.1) yielded the relation for finding $\delta\tilde{u}_{\mathrm{cr}}^2$, when all other quantities are known:

$$\dot{\varepsilon}_{\mathrm{d}} = bl\rho_{\mathrm{d}}\frac{1}{2\pi}\sqrt{-\frac{\Psi''\big(0, N(\omega)\big)}{\Psi\big(0, N(\omega)\big)}}\exp\left(-\frac{\delta\tilde{u}_{\mathrm{cr}}^2}{2\Psi(0, N(\omega))}\right), \tag{6.54}$$

$$\delta\tilde{u}_{\mathrm{cr}}\big(N(\omega)\big) = \sqrt{2\Psi\big(0, N(\omega)\big)\ln\left(\frac{bl\rho_{\mathrm{d}}}{2\pi\dot{\varepsilon}_{\mathrm{d}}}\sqrt{-\frac{\Psi''\big(0, N(\omega)\big)}{\Psi\big(0, N(\omega)\big)}}\right)}\,. \tag{6.55}$$

Finally, equality (6.11) gives σ:

$$\sigma = \sigma_{\mathrm{cr}}\left(1 - \frac{\delta\tilde{u}_{\mathrm{cr}}\big(N(\omega)\big)}{x_{\mathrm{cr}}}\right), \tag{6.56}$$

$$\Delta\sigma\big(N(\omega)\big) = \sigma_{\mathrm{ext}} - \sigma\big(N(\omega)\big)\,. \tag{6.57}$$

Theoretical and observed data for nickel were compared in terms of the following experimental parameters: applied external stress $\sigma_{\mathrm{ext}} = 68.885$ MPa, $\dot{\varepsilon}_{\mathrm{d}} = 1.19\times 10^{-4}$ s^{-1}, $b = 3.52\times 10^{-8}$ cm, the product $l\rho_{\mathrm{d}} = 435$ cm^{-1}, $U_0 = 3.34\times 10^{-19}$ J, $x_{\mathrm{cr}} = 0.2b$, $L = 3.5\times 10^{-5}$ cm, and $B = 2\times 10^{-10}$ H s cm^{-2}.

Figure 21 clearly demonstrates that our approach yields the results in excellent agreement with experimental data. The expected decrease in stress in the case of heating under thermodynamic equilibrium is several orders of magnitude smaller than in experiment, so that it proved impossible to show this value in Fig. 21. The decrease in stress $\Delta\sigma$ calculated from the data obtained should be regarded as a lower bound estimate, since the computed duration of the electric field action was taken to be several-fold shorter than that of the experimental current pulse.

7. Conclusions

Electric field action on solids by no means reduces to their heating alone. Structural defects influencing the mechanical properties of materials have electrical charges that immediately respond to applied fields and electric current passing, especially in small-sized objects, such as modern microminiature electronic devices. They can not only gradually change their state but also break down during operation, which is actually a response to an electric signal.

(1) It was shown that the application of an alternating magnetic field to vessel steel 15Kh2NMFA characterized by low plasticity and high strength after severe low-temperature deformation results in a significant (18%) decrease in yielding and a 10% increase in fracture stress, with up to 3% total elongation of the sample after destruction and up to 60% necking within a temperature range from 293 to 138 K. Simultaneously, internal friction decreases roughly two-fold and coercive force by $\approx 10\%$, whereas the dynamic shear modulus increases in the 300–500-K temperature range.

(2) Changes in the structure and physicomechanical properties related to magnetic and electric processes give rise to stress relaxation in microvolumes with a high density of internal strains (boundaries with high misorientation angles, massive dense dislocation pileups).

(3) A rationale is provided for the necessity of kinetic analysis of nonequilibrium dynamics of the crystal electron–phonon subsystem in a strong electric field [59].

(4) A method is given for the numerical solution to a system of Boltzmann kinetic equations for electron and phonon distribution functions without expanding the electron distribution function in a power series of the phonon energy [33–36].

(5) It is shown that the electron distribution function influenced by a strong electric field becomes nonequilibrium near the Fermi energy and transfers a large part of the energy to the phonon subsystem owing to electron–phonon collisions; in this way, the nonequilibrium phonon distribution function is formed. It is demonstrated, based on the modified Granato–Lücke and Landau–Gofman models with the use of the calculated phonon distribution function, that the effect of phonons on dislocations is much stronger than in the case of sample's heating under thermodynamic equilibrium by an experimentally measured temperature of 12 K [6].

(6) A comparison of calculated results and experimental data on EPE for polycrystalline nickel clearly showed that the proposed approach yields results in excellent agreement with experimental data, unlike existing methods that do not allow describing the observed events in quantitative terms.

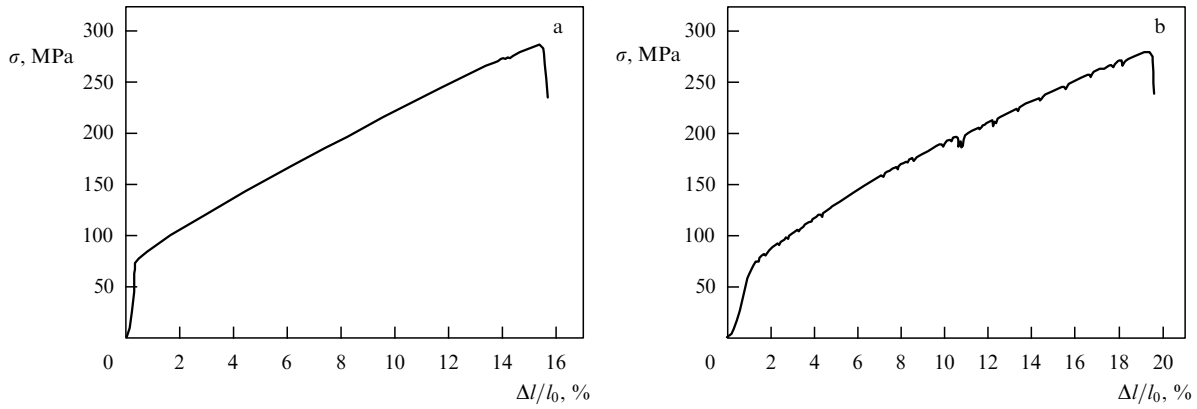

Figure 22. Strain dependence of polycrystalline Ni yield stress: (a) in the absence of additional electric field action, and (b) under periodic action of a pulsed electric current with a density of 2.75×10^5 A cm^{-2}.

(7) Softening of Ni in the creep regime under the effect of alternating and constant (including monopolar) magnetic field pulses is manifested in the region of active plastic flow known to be due to the presence of a large amount of mobile dislocations in the crystal, their movements and attachment to and detachment from the stoppers. Therefore, the causes of the influence of the magnetic field on the plastic properties of a material appear to be related to its influence on dislocation dynamic characteristics.

(8) It is known that domain boundaries becoming mobile upon re-magnetization interact with dislocations; thereby, they help them to overcome local obstacles, increase mobile dislocation density, and enhance deformation under the creep regime [55]. To rule out such an interaction, we undertook a special experimental study on the influence of an alternating magnetic field (varying in strength but not in sign) at a stable temperature (liquid-nitrogen cooling). Such an experimental design precluded the contribution of dislocation interactions with mobile domain boundaries and of thermal effects to a change in dislocation mobility upon turning on the magnetic field. It was shown in Refs [38–43, 55] that an appreciable contribution to the softening effect under the influence of a magnetic field can come from Joule heating of the sample by eddy currents upon a change in the magnetic field.

(9) Various approaches to explaining EPE are considered [63–78], each assuming absolutely different potential mechanisms behind the influence of electric current on deformation. Although the three theories are irreducible to each other, they are not mutually exclusive. By way of example, the high-rate thermal expansion observed by Bilyk, Ramesh, Unger et al. [67, 68] does not forbid the influence of the magnetic field on impurity and nucleus spins of fastened dislocations, as postulated in the Molotskii model [64–66]. Nor are other possible mechanisms excluded. For example, none of the above theories contradicts reports on the enhanced production by nonequilibrium electrons of short-wavelength phonons, which, in turn, effectively detach dislocations from stoppers; hence, the necessity of further experimental studies to either confirm or refute a concrete theory. Planning such experiments should envisage addressing the following important issues:

— differentiation between rapid heating and electromagnetic influence to verify the Bilyk et al. model [67, 68];

— experimenting with materials free from paramagnetic impurities to verify the Molotskii model [64–66].

(10) To evaluate the contribution from the inductive component of an electric field, resulting from a change in induction of a monopolar magnetic field, S V Lebedev (V N Karazin Kharkiv National University) undertook an experimental study on the influence of pulsed electric current density on the reduction in yield stress. Comparative experiments were carried out with identical samples of highly purified polycrystalline Ni (99.996%). Parameters of electric current density corresponded to the strength of inductive electric field generated by monopolar pulses of the magnetic field under creep conditions (see Sections 4, 6). Figure 22b shows that a current pulse decreases the yield stress by approximately 1%, which corresponds to 0.1% deformation. These experimental data correlate with structural changes (see Fig. 21).

(11) The following studies are absolutely indispensable:

(a) comprehensive experimental and theoretical studies, along with the development of a physical and mathematical model for the description of nonstationary nonequilibrium kinetics of the crystal electron–phonon subsystem in electric and/or magnetic fields, taking into consideration the excitation of plasmonic solitons, breathers, and other nonlinear entities;

(b) construction of a physical model for the quantitative description of the influence of nonstationarity and departure from equilibrium of electron and phonon distribution functions on the structural changes in crystals altering their physicomechanical properties, with due regard for the excitation of nonlinear entities;

(c) experimental studies, validation of the constructed physical model, and a description (with due regard for the excited nonlinear entities) of the influence of nonstationarity and nonequilibrium behavior of electron and phonon distribution functions on the structural changes in crystals caused by the behavior of point and extended defects in the lattice, determining their thermal, electric, and other macroscopic characteristics, including plasticity and hardness, with the proper interpretation of experimental data.

References

1. Hayashi S, Takahashi S, Yamamoto M *J. Phys. Soc. Jpn.* **25** 910 (1968)
2. Gindin I A, Lavrinenko I S, Neklyudov I M *JETP Lett.* **16** 241 (1972); *Pis'ma Zh. Eksp. Teor. Fiz.* **16** 341 (1972)

3. Troitskii O A, Likhtman V I *Sov. Phys. Dokl.* **8** 91 (1963); *Dokl. Akad. Nauk SSSR* **148** 332 (1963)
4. Gromov V E, Tsellermaier V Ya, Bazaikin V I *Elektrostimulirovannoe Volochenie*: *Struktura i Analiz* (Electrically Enhanced Drawing: Structure and Analysis) (Moscow: Nedra, 1996)
5. Spitsyn V I, Troitskii A *Elektroplasticheskaya Deformatsiya Metallov* (Electroplastic Deformation of Metals) (Moscow: Nauka, 1985)
6. Troitskii A et al. *Fizicheskie Osnovy Obrabotki Sovremennykh Materialov* (*Teoriya, Tekhnologiya, Struktura i Svoistva*) (Physical Principles of Metal Processing (Theory, Technology, Structure, and Properties)) Vol. 1 (Moscow–Izhevsk: Izd. Inst. Komp. Issled., 2004)
7. Neklyudov I M, Starodubov Ya D, Sokolenko V I *Ukr. Fiz. Zh.* **50** (8A) A113 (2005)
8. Neklyudov I M, Azhazha V M, Yushchenko K A, Sokolenko V I, Mats A V, Netesov V M, Varganov V V *Fiz. Khim. Obrab. Mater.* (1) 84 (2011)
9. Vasil'ev M A *Usp. Fiz. Met.* **8** (1) 65 (2007)
10. Sokolenko V I, Mats A V, Karas' V I, Okovit V S , Chernyak N A, Gorbatenko V M *J. Low Temp. Phys.* **41** 399 (2015)
11. Neklyudov I M et al., in *Trudy 18 Mezhdunarod. Konf. po Fizike Radiatsionnykh Yavlenii i Radiatsionnomu Materialovedeniyu* (Proc. of the 18th Intern. Conf. on Physics of Radiation Phenomena and Radiative Materials Science) (Kharkov: NNTs KhFTI, 2008) p. 156
12. Alshits V I et al. *Phys. Usp.* **60** 305 (2017); *Usp. Fiz. Nauk* **187** 327 (2017)
13. Trefilov V I et al. *Deformatsionnoe Uprochnenie i Razrushenie Polikristallicheskikh Metallov* (Deformation Hardening and Destruction of Polycrystalline Metals) (Kiev: Naukova Dumka, 1989)
14. Krainyuk E A et al. *Voprosy Atom. Nauki Tekh. Fiz. Radiatsionnykh Povrezhdenii Radiatsionnoe Materialoved.* (3) 165 (2004)
15. Neklyudov I M, Sokolenko V I, Tkachenko V I, in *Trudy 9-i Mezhdunarod. Konf. "Fizicheskie Yavleniya v Tverdykh Telakh", Kharkov, 2009* (Proc. of the 9th Intern. Conf. "Physical Phenomena in Solids"), p. 93
16. Sosin A, Kifer D V, in *Mikroplastichnost'* (Microplasticity) (Moscow: Metallurgiya, 1972) p. 130
17. Mitsek A I, Pushkar' V N *Real'nye Kristally s Magnitnym Poryadkom* (Real Crystals with Magnetic Order) (Kiev: Naukova Dumka, 1978)
18. Dubinko V I et al. *Voprosy Atom. Nauki Tekh. Fiz. Radiatsionnykh Povrezhdenii Radiatsionnoe Materialoved.* (4–2) 158 (2009)
19. Zakharov V E, Karas' V I *Phys. Usp.* **56** 49 (2013); *Usp. Fiz. Nauk* **183** 55 (2013)
20. Zakharov V E, in *Basic Plasma Physics* (Handbook of Plasma Physics, Vol. 2, Eds A A Galeev, R N Sudan) (Amsterdam: North-Holland, 1984) p. 3; in *Osnovy Fiziki Plazmy* (Basic Plasma Physics) Vol. 2 (Eds A A Galeev, R Sudan) (Moscow: Energoatomizdat, 1984) p. 48
21. Zakharov V E *J. Appl. Mech. Tech. Phys.* **6** (4) 22 (1965); *Zh. Prikl. Mekh. Tekh. Fiz.* (4) 35 (1965)
22. Zakharov V E, Filonenko N N *Sov. Phys. Dokl.* **11** 881 (1967); *Dokl. Akad. Nauk SSSR* **170** 1292 (1966)
23. Zakharov V E, Filonenko N N *J. Appl. Mech. Tech. Phys.* **8** (5) 37 (1967); *Zh. Prikl. Mekh. Tekh. Fiz.* (5) 62 (1967)
24. Zakharov V E *Sov. Phys. JETP* **24** 740 (1967); *Zh. Eksp. Teor. Fiz.* **51** 688 (1966)
25. Zakharov V E, Sagdeev R Z *Sov. Phys. Dokl.* **15** 439 (1970); *Dokl. Akad. Nauk SSSR* **192** 297 (1970)
26. Zakharov V, Dias F, Pushkarev A *Phys. Rep.* **398** 1 (2004)
27. Zakharov V E (Ed.) *Nonlinear Waves and Weak Turbulence* (American Mathematical Society Translations, Ser. 2, Vol. 182) (Providence, RI: American Mathematical Society, 1998)
28. Musher S L, Rubenchik A M, Zakharov V E *Phys. Rep.* **252** 177 (1995)
29. Zakharov V E, L'vov V S, Falkovich G *Kolmogorov Spectra of Turbulence I. Wave Turbulence* (Berlin: Springer-Verlag, 1992)
30. Kontorovich V M *Radiofiz. Radioastron.* **11** 5 (2006)
31. Kats A V et al. *Sov. Phys. JETP* **44** 93 (1976); *Zh. Eksp. Teor. Fiz.* **71** 177 (1976)
32. Karas' V I, Moiseev S S, Novikov V E *Sov. Phys. JETP* **44** 744 (1976); *Zh. Eksp. Teor. Fiz.* **71** 1421 (1976)
33. Karas' V I et al., in *The Intern. Conf. MSS-14*: *Mode Conversion, Coherent Structure and Turbulence, 24–27 November 2014, Conf. Proc.* (Moscow: LENAND, 2014) p. 64
34. Zakharov V E, Karas' V I, Vlasenko A M, in *The Intern. Conf. MSS-14*: *Mode Conversion, Coherent Structure and Turbulence, 24–27 November 2014, Conf. Proc.* (Moscow: LENAND, 2014) p. 34
35. Karas' V I, Vlasenko A M, Voyevodin V N, Sokolenko V I, Zakharov V E *East Eur. J. Phys.* **1** (3) 40 (2014)
36. Karas' V I, Vlasenko A M, Sokolenko V I, Zakharov V E *JETP* **121** 499 (2015); *Zh. Eksp. Teor. Fiz.* **148** 573 (2015)
37. Karas' V I, Potapenko I F *Voprosy Atom. Nauki Tekh. Fiz. Radiatsionnykh Povrezhdenii Radiatsionnoe Materialoved.* (4–2) 150 (2009)
38. Gindin I A, Kravchenko S F, Starodubov Ya D *Prib. Tekh. Eksp.* (3) 269 (1963)
39. Aksenov V K et al. *Fiz. Nizk. Temp.* **6** (1) 118 (1980)
40. Aksenov V K et al. *Fiz. Nizk. Temp.* **3** (7) 922 (1977)
41. Gindin I A, Lavrinenko I S, Neklyudov I M *Sov. Phys. Solid State* **15** 451 (1973); *Fiz. Tverd. Tela* **15** 636 (1973)
42. Chow C R, Nembach E *Acta Metallurg.* **24** 453 (1976)
43. Aksenov V K et al. *Fiz. Nizk. Temp.* **4** 1316 (1978)
44. Bol'shutkin D N, Desnenko V A, Il'ichev V Ya *Fiz. Nizk. Temp.* **2** 256 (1976)
45. Bol'shutkin D N, Desnenko V A, Il'ichev V Ya *Fiz. Nizk. Temp.* **2** 1544 (1976)
46. Dovbnya A N, Sokolenko V I, Karaseva E V, Mats A V, Mats V A, Savchuk E S *Voprosy Atom. Nauki Tekh. Fizika Radiatsionnykh Povrezhdenii Radiatsionnoe Materialoved.* (2) 39 (2014)
47. Karas' V I, Sokolenko V I, Karasyova E V, Mats A V, Vlasenko A M *Voprosy Atom. Nauki Tekh. Fizika Radiatsionnykh Povrezhdenii Radiatsionnoe Materialoved.* (4) 277 (2015)
48. Karas' V I, Vlasenko A M, Zakharov V E, in *Proc. VI Intern. Conf. for Young Scientists "Low Temperature Physics", ICYS LTP 2015, Kharkov, 2015*, p. 51
49. Zakharov V E, Karas' V I, in *Problemy Teoreticheskoi Fiziki. Nauchnye Trudy* (Problems of Theoretical Physics: Scientific Works) Issue 1 (Kharkov: KhNU im. V N Karazina, 2014) p. 248
50. Karas' V I et al. *Metallofiz. Noveish. Tekhnol.* **38** 1024 (2016)
51. Spitsyn V I, Troitskii O A *Vestn. Akad. Nauk SSSR* (11) 10 (1974)
52. Neklyudov I M, Kamyshanchenko N V *Fizicheskie Osnovy Prochnosti i Plastichnosti Metallov* (The Physical Basis of Metal Strength and Plasticity) Pt. 2 *Defekty v Kristallakh* (Defects in Crystals) (Moscow–Belgorod: Izd. Belgorod. Gos. Univ., 1997)
53. Landau A I, Gofman Yu I *Sov. Phys. Solid State* **16** 2220 (1975); *Fiz. Tverd. Tela* **16** 3427 (1974)
54. Granato A, Lücke K *J Appl. Phys.* **27** 583 (1956)
55. Kaganov M I, Kravchenko V Ya, Natsik V D *Sov. Phys. Usp.* **16** 878 (1974); *Usp. Fiz. Nauk* **111** 655 (1973)
56. Perrin N, Budd H *Phys. Rev. Lett.* **28** 1701 (1972)
57. Bass F G, Gurevich Yu G *Goryachie Elektrony i Sil'nye Elektromagnitnye Volny v Plazme Poluprovodnikov i Gazovogo Razryada* (Hot Electrons and Strong Electromagnetic Waves in Plazma of Semiconductors and Gas Discharge) (Moscow: Nauka, 1975)
58. Silin V P *Vvedenie v Kineticheskuyu Teoriyu Gazov* (Introduction to the Kinetic Theory of Gases) 3rd ed., rev. and correct. (Moscow: LIBROKOM, 2013)
59. Lifshitz E M, Pitaevskii L P *Physical Kinetics* (Oxford: Pergamon Press, 1981); Translated from Russian: *Fizicheskaya Kinetika* (Moscow: Fizmatlit, 2002)
60. Karas' V I, Potapenko I F, Vlasenko A M *Voprosy Atom. Nauki Tekh. Plazmennaya Electron. Novye Metody Uskoreniya* (4) 272 (2013)
61. Karas' V I, Vlasenko A M, Sokolenko V I, in *Materialy 55-i Mezhdunarod. Konf.* "*Aktual'nye Problemy Prochnosti*" (Proc. of the 55th Intern. Conf. "Actual Problems of Strength") (Kharkov: NNTs KhFTI, 2014) p. 14
62. Lebedev V P, Savich S V *Vestn. Kharkov. Nats. Univ. Fiz.* **962** (15) 88 (2011)

63. Sprecher A F, Mannan S L, Conrad H *Acta Metallurg.* **34** 1145 (1986)
64. Molotskii M, Fleurov V *Phys. Rev. B* **52** 15829 (1995)
65. Molotskii M, Fleurov V *Phys. Rev. Lett.* **78** 2779 (1997)
66. Molotskii M I *Mater. Sci. Eng. A* **287** 248 (2000)
67. Bilyk S R, Ramesh K T, Wright T W *J. Mech. Phys. Solids* **53** 525 (2005)
68. Unger J et al., in *Proc. of the 2nd Intern. Conf. on High Speed Forming, Dortmund, 2006*, p. 23
69. Stolyarov V V *Bull. Russ. Acad. Sci. Phys.* **79** 1165 (2015); *Izv. Ross. Akad. Nauk Ser. Fiz.* **79** 1314 (2015)
70. Stolyarov V V *Bull. Russ. Acad. Sci. Phys.* **78** 234 (2014); *Izv. Ross. Akad. Nauk Ser. Fiz.* **78** 357 (2014)
71. Stolyarov V V *Vestn. Nauchno-Tekh. Razvitiya* (3) 35 (2013)
72. Conrad H *Mater. Sci. Eng. A* **287** 276 (2000)
73. Stolyarov V et al. *J. High Pressure Phys. Technol.* **4** (16) 64 (2006)
74. Medentsov V E, Stolyarov V V *Deform. Razrush. Material.* (12) 37 (2012)
75. Stolyarov V V *Bull. Russ. Acad. Sci. Phys.* **76** 96 (2012); *Izv. Ross. Akad. Nauk Fiz.* **76** 108 (2012)
76. Stolyarov V V, Ugurchiev U Kh *Fiz. Tekh. Vys. Davl.* **19** 92 (2009)
77. Fedotkin A A, Medentsov V E, Stolyarov V V *Izv. Vyssh. Uchebn. Zaved. Chern. Metal.* **55** (8) 47 (2012)
78. Zuev L B, Danilov V I *Fizicheskie Osnovy Prochnosti Materialov* (The Physical Basis of Material Strength) 2nd ed. (Dolgoprudnyi: Intellekt, 2016)